

23 **Abstract:** Accurate delineation of lake surface area is fundamental for understanding
24 eco-hydrological processes in arid regions, yet long-term lake records are often
25 constrained by cloud contamination, seasonal ice cover, and data gaps. In this study, we
26 develop an optimized lake-area extraction framework that integrates seasonal water-
27 index selection, adaptive threshold segmentation, maximum connected-component
28 analysis, and mutual-information-based image gap filling to construct a continuous
29 monthly lake-area time series for Bahannao Lake from 1984 to 2024. This framework
30 substantially improves the temporal continuity and robustness of long-term monitoring
31 for small lakes in arid environments, and its regional applicability is further validated
32 through comparative analyses with Hongjiannao Lake and Wuliangsuhai Lake. Based
33 on the reconstructed time series, we quantitatively assess the multi-climatic controls on
34 lake-area variability by combining correlation analysis with an XGBoost model. The
35 results reveal pronounced seasonal differences and distinct stage-dependent evolution
36 in lake dynamics, with the dominance alternating between precipitation-driven water
37 input and evaporative demand across different temporal scales. Our findings highlight
38 the nonlinear hydro-climatic responses of arid-region lakes to climate variability and
39 provide both technical support and scientific insight for long-term lake monitoring and
40 water-resource management in dryland regions.

41 **Keywords:** remote sensing, lake area extraction, XGBoost, arid region, hydro-climate

42

43

44 **1 Introduction**

45 Over the past century, with the intensification of global climate change and the
46 increasing human ability to modify nature, the impact of climate change on lake
47 systems and the surrounding water environment has become more pronounced. The
48 formation and disappearance, expansion and contraction of lakes, as well as changes in
49 water and ecological environments, are the result of interactions among global, regional,
50 and local tectonic activities, climate events, and human activities. Within these systems,
51 a series of complex interactions drive the evolution of lake systems (Ma et al., 2020).

52 Lakes are vital natural resources that are highly sensitive to climate change
53 (Adrian et al., 2009; Schmid et al., 2014). Globally, there are over 100 million lakes,
54 which store 87% of the Earth's liquid surface freshwater. Climate change is one of the
55 most severe threats to global lake ecosystems. As observed in recent decades, lake
56 surface conditions—such as ice cover, surface temperature, evaporation, and water
57 levels—have responded significantly to this threat (Woolway et al., 2020; Tong et al.,
58 2023). Approximately 53% of the world's lakes have experienced a decline in water
59 storage, with a reduction of about 22 billion tons per year. Climate change and human
60 water use have primarily driven the net decrease in water volume in approximately 100
61 large natural lakes worldwide. Lakes in both arid and humid regions are experiencing
62 water loss, with drying trends being more widespread than previously understood.
63 Despite the shrinking of most lakes globally, 24% of lakes and reservoirs have shown
64 a significant increase in water storage. These lakes and reservoirs are mostly located in
65 sparsely populated regions, such as the Tibetan Plateau and the northern Great Plains

66 of North America, as well as areas with newly constructed reservoirs, including the
67 Yangtze River, Mekong River, and Nile River basins (Pickens et al., 2020).

68 China has a vast territory with an extensive network of rivers and lakes. There are
69 2693 lakes with an area greater than 1 km², among which 2557 lakes (95% of the total)
70 have an area between 1 and 100 km². Additionally, there are 10 exceptionally large
71 lakes with an area exceeding 1000 km². The total lake area in China has shown a
72 significant increasing trend, expanding by approximately 7858.53 km² (11.41%) over
73 the past 30 years (Ma et al., 2010; Ma et al., 2011). However, the spatial and temporal
74 imbalance of water resources has intensified, with notable differences in trends across
75 various lake regions. The lake areas in the Tibetan Plateau and Xinjiang regions have
76 increased significantly, contributing 111.55% and 28.41% of the national lake area
77 growth, respectively. In contrast, the lake areas in the Eastern Plain, Inner Mongolia
78 Plateau, Northeast Plain and Mountainous Region, and Yunnan-Guizhou Plateau have
79 declined significantly, with reductions of 24.53%, 9.30%, 6.06%, and 0.54%,
80 respectively. Among these, the Mongolian-Xinjiang Plateau experienced the largest
81 decline in lake numbers, with a loss of 111 lakes. Some lakes in this region have shown
82 signs of shrinkage and salinization (Yang et al., 2010). However, despite increasing
83 attention to global lake changes, small and medium-sized closed-basin lakes in arid and
84 semi-arid regions remain poorly characterized in long-term observations. These lakes
85 are highly sensitive to climate variability but are often underrepresented in existing
86 global or regional datasets, highlighting an urgent need for improved long-term
87 monitoring.

88 Scientists have discovered that the abrupt change timing of river and lake systems
89 varies significantly across different latitudes and altitudes (Råman Vinnå., 2021; Zhou
90 et al., 2021). Mountain and polar lakes tend to experience abrupt changes earlier than
91 temperate and tropical river-lake systems (Jeppesen et al, 2014). Additionally, under
92 varying levels of human impact, the timing of abrupt changes in lakes also differs.
93 Lakes in regions with low human impact generally experience abrupt changes earlier
94 than those in areas with strong human influence (Preston et al., 2016). Analysis of the
95 driving factors of lake abrupt changes indicates that the causes vary. Before the 1950s,
96 climate change was the primary factor controlling abrupt changes in lake ecosystems.
97 However, after the 1950s, both climate change and human disturbances became
98 dominant factors. In temperate and tropical regions with strong human influence, lake
99 changes are mainly driven by nutrient enrichment and pollution. In contrast, lakes
100 located in high-altitude and high-latitude regions, which are less affected by human
101 activities, are more vulnerable to climate change. Furthermore, the interaction of
102 multiple drivers increases the likelihood of abrupt changes in lakes, with climate change
103 being the most frequently interacting factor leading to transformations in river-lake
104 ecosystems (Vincent et al., 2009.). Li et al. (2025) pointed out that seasonality is the
105 dominant driver of lake-surface-extent variations globally

106 For example, Plug et al.(2008) investigated lake area changes in the Tuktoyaktuk
107 Peninsula in northwest Canada. They found that from 1978 to 1992, the total lake area
108 increased, while from 1992 to 2001, the total lake area decreased. Their study identified
109 precipitation as the main factor driving these changes. Similarly, Carroll et al. (2011)

110 studied the lake area changes in high-latitude northern Canada and discovered that lake
111 areas showed a significant decline, exhibiting regional clustering characteristics, with
112 climate factors driving these changes. Labazhuoma et al. (2017) explored the expansion
113 of Tangra Yum Co from 1977 to 2014. Their results indicated that, under the background
114 of climate warming, the combined effects of glacier melt, precipitation increase, and
115 evaporation changes contributed to the lake's expansion. Likewise, Li Meng et al. (2017)
116 examined the changes in the water surface area and water storage of Nam Co from 1976
117 to 2015. Their findings showed that the water surface area and water storage of Nam
118 Co continued to increase, with the fastest growth in water storage occurring between
119 1997 and 2009. The study concluded that the primary factor driving the increase in Nam
120 Co's water volume was glacier melt, followed by increased precipitation and reduced
121 evaporation.

122 However, the precise measurement of lake area remains a major constraint for
123 analyzing lake changes. With advancements in science and technology, remote sensing
124 has provided a unique and effective method for monitoring the spatiotemporal
125 variations in surface water areas on broad geographic scales (Liu et al., 2020).

126 Currently, water extraction methods using optical sensors have been widely
127 applied²⁸⁻³⁰ (McFeeters 1996; Yao et al., 2015; Donchyts et al., 2016). However,
128 existing water body area products often fail to meet ideal spatial or temporal resolution
129 requirements³¹⁻³² (Cooley et al., 2017; Huang et al., 2018). For example, the 2016
130 Global Climate Observing System (GCOS) Implementation Plan recommended a
131 resolution of 20 meters and a daily monitoring frequency (Secretariat, 2009). High-

132 temporal-resolution sensors, such as the Moderate Resolution Imaging
133 Spectroradiometer (MODIS) onboard Terra and Aqua satellites, have been used to
134 assess water body areas at time scales ranging from daily to 16-day intervals (Bergé-
135 Nguyen et al., 2015; Wang et al., 2018). However, many small water bodies (e.g., 10–
136 50 km² or smaller) and irregularly shaped larger water bodies may not be accurately
137 distinguished using coarse-resolution MODIS images (250–500 meters in the visible
138 and near-infrared bands) (Tao et al., 2015). Compared with MODIS, Landsat images
139 (e.g., Landsat 5 Thematic Mapper (TM), Landsat 7 Enhanced Thematic Mapper Plus
140 (ETM+), and Landsat 8 Operational Land Imager (OLI)) offer higher spatial resolution
141 (30 meters) and a temporal resolution of 16 days (or better when combining multiple
142 Landsat sensors). However, due to cloud contamination (Rossow et al., 1999), the
143 actual temporal frequency of water body mapping based on Landsat is often much lower
144 than the nominal resolution and may extend to a year for lakes with persistent ice cover
145 (Yao et al., 2018). The recently launched Sentinel-2A and 2B satellites, equipped with
146 Multispectral Instruments (MSI), provide a resolution of 10 meters in the visible and
147 near-infrared bands, with a revisit period of 5–10 days. However, their observations
148 currently cover only the past few years (since 2015) and are not yet suitable for long-
149 term decadal monitoring.

150 Beyond the trade-offs between spatial and temporal resolution, several other
151 factors challenge high-resolution monitoring of long-term global surface water area
152 changes (Klein et al., 2017). These include the inherent spectral heterogeneity of water,
153 atmospheric influences (clouds and aerosols), topographic shadows, aquatic vegetation,

154 and spectral contamination from ice/snow cover. In such complex conditions,
155 integrating multiple techniques is often necessary to achieve robust water body
156 extraction.

157 Recently, Pekel et al. (2014) utilized a large training dataset, combined with expert
158 systems and visual analysis, to identify the presence or absence of water on a monthly
159 basis for each pixel in archival Landsat images from 1984 to 2015. This product was
160 named the Joint Research Centre (JRC) Global Surface Water dataset (hereinafter
161 referred to as GSW). Despite its significant achievements, GSW is based on cloud-free
162 pixels, meaning that the mapped extent of specific water bodies is only complete when
163 monthly composite images have minimal cloud cover. A follow-up study by Busker et
164 al. (Buske et al., 2019) used a subset of the GSW dataset, selecting images with cloud
165 cover below 5%, to extract the monthly area of 137 lakes/reservoirs. For nearly half of
166 these lakes/reservoirs, the correlation between area and radar altimetry-measured water
167 levels exceeded 0.8. However, the temporal frequency of the resulting area time series
168 was still constrained by the availability of cloud-free images, and due to the current
169 availability of GSW, the time series was interrupted after October 2015. One potential
170 method to increase the temporal frequency of lake mapping based on Landsat data is to
171 estimate water surface area from contaminated images (e.g., those affected by clouds
172 or observation gaps). Although these images are of relatively lower quality, the exposed
173 portions of lakes within them may provide useful information for inferring the complete
174 extent. For instance, Zhao and Gao (2018) applied the monthly water mapping data
175 from the GSW dataset to generate area time series for 6,817 reservoirs worldwide from

176 1984 to 2015. Their method involved recovering complete reservoir extents from cloud-
177 contaminated images by segmenting pixels based on the water occurrence probability
178 provided in the GSW dataset. Compared to the results of Busker et al., their generated
179 area time series increased the number of observations by approximately 80%. However,
180 the reliance on the existing GSW dataset restricted their reservoir area records to the
181 1984–2015 period, and the validation of their recovery method was limited to only nine
182 reservoirs with significant water level variations. These studies demonstrate the
183 feasibility of large-scale lake monitoring, but also highlight persistent limitations
184 related to temporal continuity, cloud dependence, and the applicability of existing
185 products to small lakes. As a result, many existing lake-area studies rely on annual or
186 seasonal snapshots derived from a limited number of cloud-free images, which may
187 obscure important intra-annual variability, abrupt changes, and short-term climate
188 responses, particularly for small lakes with strong seasonal dynamics.

189 To address this limitation, we construct a continuous 40-year monthly lake-area
190 time series for Bahannao Lake by integrating multi-source Landsat imagery and
191 applying a tailored image-processing workflow. This higher-temporal-resolution
192 dataset enables a more detailed assessment of seasonal and interannual lake dynamics.

193 Bahannao Lake is a small closed-basin lake located in a semi-arid desert region of
194 northern China. Owing to its remote location and the long-term absence of systematic
195 in situ observations, continuous records of lake area are lacking. Nevertheless, as a
196 water body embedded in a fragile desert ecosystem, variations in lake area are highly
197 sensitive to hydro-climatic changes and play an important role in regional eco-

198 hydrological stability.

199 In recent decades, intensified warming and drying have caused pronounced lake
200 shrinkage, characterized by strong interannual variability and multiple abrupt changes.
201 However, compared with larger or well-monitored lakes, the dynamic behavior and
202 driving mechanisms of Bahannao Lake remain poorly understood due to the lack of
203 long-term, high-temporal-resolution observations. As a typical but underrepresented
204 small lake in arid regions, Bahannao Lake provides an ideal case for testing robust
205 remote-sensing monitoring methods and investigating hydro-climatic controls on
206 dryland lake dynamics.

207 Despite substantial progress in global lake monitoring, significant gaps remain for
208 lakes in arid and semi-arid regions. Long-term and continuous lake area records are
209 often interrupted by cloud contamination, seasonal ice cover, and striping artifacts,
210 while the role of hydro-climatic drivers—particularly their nonlinear interactions—
211 remains insufficiently understood.

212 To address these challenges, this study develops an optimized lake area extraction
213 framework that integrates seasonal index selection, adaptive thresholding, connectivity
214 analysis, and mutual information–based gap filling to construct a continuous monthly
215 lake-area record for Bahannao Lake from 1984 to 2024. By coupling this reconstructed
216 time series with multi-factor analysis using the XGBoost model, we quantify the
217 relative importance and nonlinear effects of key hydro-climatic drivers on lake
218 dynamics. This framework not only improves the reliability of long-term lake
219 monitoring under complex conditions, but also provides new insights into seasonal and

220 interannual climate controls on small lakes in arid and semi-arid regions.

221 **2 Data and Methods**

222 **2.1 Study area and data**

223 Closed-basin lakes of various sizes are widely distributed across the Ordos Plateau,
224 formed since the late Quaternary through combined aeolian and fluvial erosion
225 processes. Bahannao Lake is the terminal basin of a chain of seven bead-like erosional
226 lake depressions that developed along an ancient river valley. Bahannao Lake
227 (109°16'E, 39°19'N) is located in the central Ordos Plateau at an elevation of 1278 m,
228 with a lake-basin area of 26.50 km². The basin is underlain by a continuous and intact
229 Lower Cretaceous sandstone formation, which provides a closed geomorphic setting
230 primarily recharged by atmospheric precipitation. The sandstone contains abundant
231 sodium- and calcium-rich carbonates, serving as the major source of dissolved salts in
232 Bahannao Lake. Administratively, the study area belongs to Wushen Banner of the
233 Ordos region in Inner Mongolia (Figure 1).

234 The zonal vegetation is dominated by arid to semi-arid desert steppe. The region
235 is controlled for most of the year by the northwesterly monsoon, resulting in a cold and
236 dry climate, while the southeasterly monsoon occasionally influences the area and plays
237 a decisive role in seasonal precipitation. The mean annual temperature ranges from 6 to
238 9 °C, and the mean annual precipitation is only 200–300 mm, concentrated mainly from
239 June to September with short-duration high-intensity rainfall events. In contrast, the
240 annual potential evaporation reaches 2500–3000 mm, approximately ten times the
241 precipitation amount, and the regional aridity index ranges from 3.5 to 4.0.

242 Because of the extremely fragile water balance and rapid hydrological response to
243 climatic anomalies, Bahannao Lake and other nearby lakes are widely recognized as
244 important natural indicators of climate variability, drought intensification, and land–
245 atmosphere interactions in the arid and semi-arid regions of northern China.

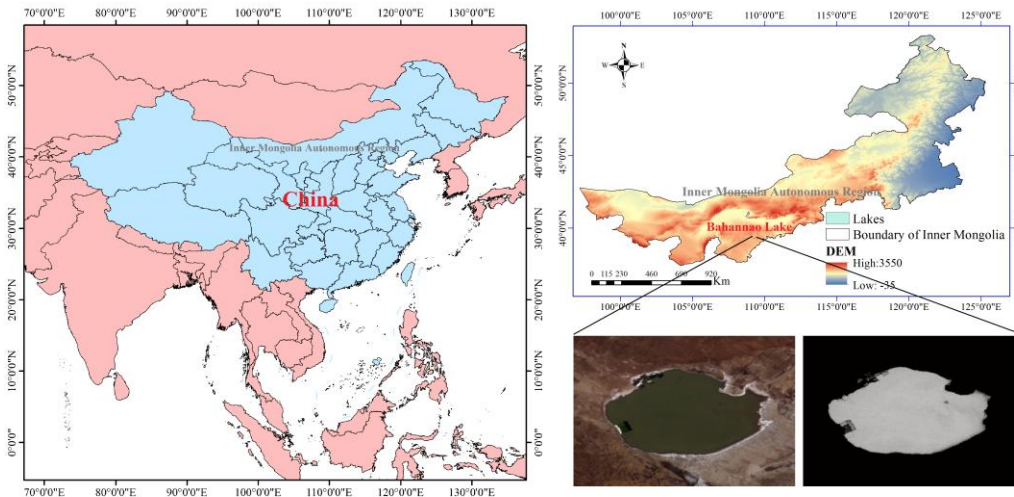
246 This study utilizes remote sensing imagery from the Landsat 5 TM, Landsat 7 TM,
247 and Landsat 8 OLI sensors, specifically using atmospherically corrected reflectance
248 data (Tier 1 TOA Reflectance). Tier 1 data is selected due to its highest quality, making
249 it suitable for time-series analysis and studies on global surface water extent and
250 dynamics. The Landsat 5 TM imagery covers the period from 1984 to 2011, while
251 Landsat 8 imagery spans from 2013 to 2023. Since imagery for 2012 is missing in both
252 datasets, Landsat 7 TM is used as a supplement. However, Landsat 7 TM imagery
253 exhibits significant striping artifacts, which were avoided as much as possible during
254 data selection.

255 For hydro-climatic elements, this study employs the fifth-generation atmospheric
256 reanalysis dataset from ECMWF (European Centre for Medium-Range Weather
257 Forecasts), covering global climate data from January 1950 to the present. The dataset
258 has a temporal resolution of daily and a spatial resolution of $0.1^\circ \times 0.1^\circ$. The hydro-
259 climatic variables used in this study include precipitation (P, mm), air temperature at 2
260 m (T, °C), 2 m dew point temperature (Td, °C), relative humidity (RH, %), potential
261 evapotranspiration (PET, mm), net shortwave radiation at the surface (msnswrf, $W\ m^{-2}$),
262 net longwave radiation at the surface (msnlwrf, $W\ m^{-2}$), surface latent heat flux (mslhf,
263 $W\ m^{-2}$), and surface sensible heat flux (msshf, $W\ m^{-2}$). These variables jointly

264 characterize atmospheric moisture conditions, energy balance, and evaporative demand
265 in the study region.

266

267



268 Figure 1 Overview map of the study area. Source: U.S. Geological Survey (USGS). Data are
269 in the public domain.

270 2.2 Methods

271 2.2.1 Optimized lake area extraction method

272 Although water-index-based lake extraction from Landsat imagery is well
273 established, long-term monthly monitoring of small lakes in arid regions poses specific
274 challenges, including frequent cloud contamination, striping artifacts in ETM+ data,
275 and strong intra-annual variability. To address these issues, we developed an optimized
276 processing workflow tailored to long-term monthly lake monitoring.

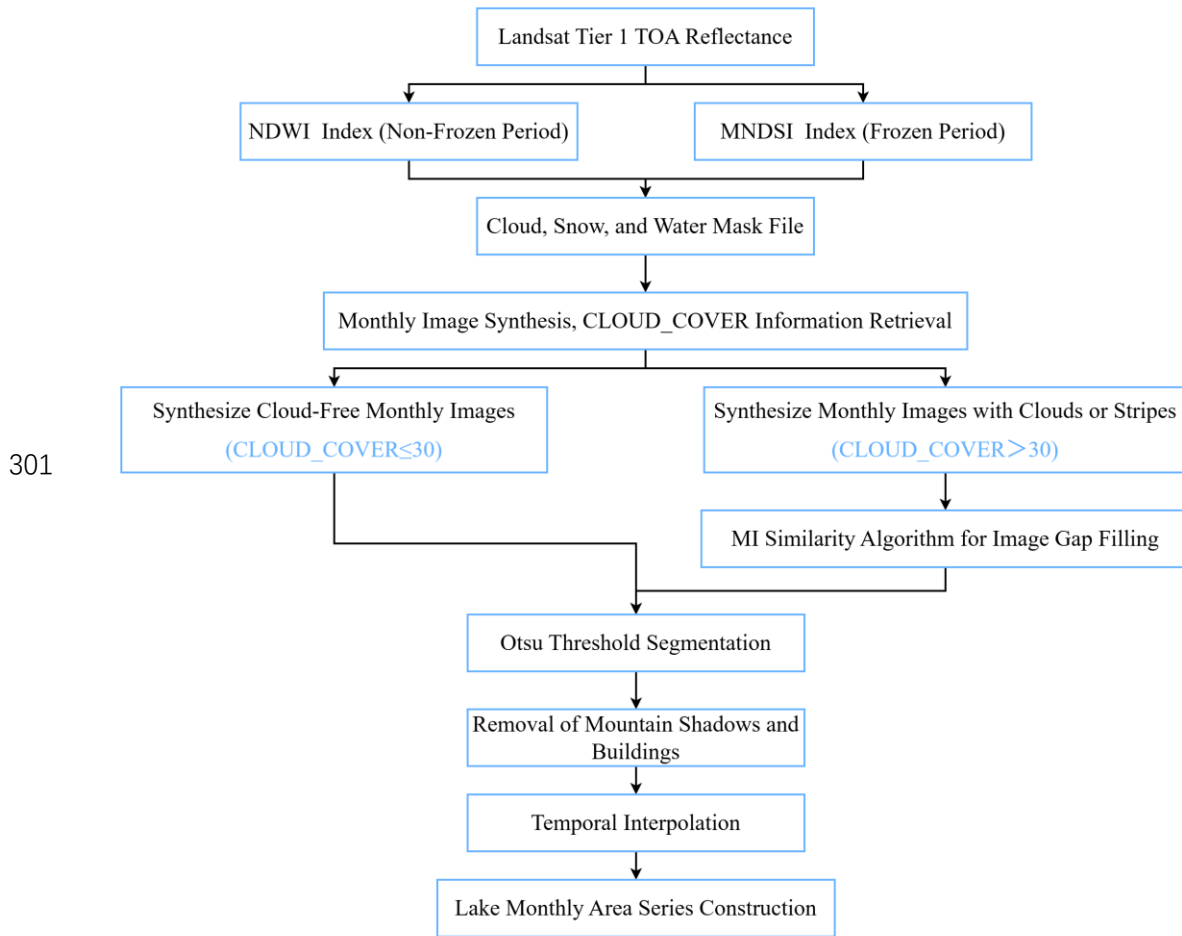
277 This study employs 30-meter full-atmosphere imagery from the Landsat 5
278 Thematic Mapper (TM), Landsat 7 Enhanced Thematic Mapper Plus (ETM+), and
279 Landsat 8 Operational Land Imager (OLI) satellites to derive monthly lake area

280 estimates for the study region from January 1984 to December 2024.

281 Different lake remote sensing indices were selected for non-freezing and freezing
282 periods, respectively. For non-freezing periods, remote sensing indices were processed
283 to remove cloud and snow interference. Images were filtered based on cloud cover
284 percentage (C), and monthly composite images were generated. The Otsu thresholding
285 method was then applied to automatically determine segmentation thresholds. To
286 distinguish between lakes and mountainous areas, a digital elevation model (DEM) was
287 used, setting the slope (θ) and aspect (ϕ) thresholds to 0.

288 Considering that most lakes exhibit connectivity, this study adopts the maximum
289 connected component analysis algorithm from the OpenCV computer vision library to
290 delineate lake boundaries. Images were categorized based on cloud cover information
291 ('CLOUD_COVER'): those with cloud cover $\leq 30\%$ were classified as cloud-free
292 images, while the remaining images were considered cloudy. For cloudy images, the
293 MI (Mutual Information) algorithm was used to match them with the most similar
294 cloud-free images. The most similar image was then merged with the original cloudy
295 image to generate a filled version.

296 For images with striping artifacts, the same filling method was applied as for
297 cloudy images. Clear lake boundaries from historical cloud-free images were used, and
298 the MI algorithm was employed to find the most similar historical cloud-free images
299 for filling missing water pixels in striped areas, ultimately obtaining the final lake water
300 extent. The specific process is shown in Figure 2.



302 Figure 2 Flowchart of lake area extraction process

303 2.2.2 Aridity index (AI)

304 The aridity index (AI) was used to quantify regional drought conditions. AI is
 305 defined as the ratio of precipitation (P) to potential evapotranspiration (PET), expressed
 306 as:

307
$$AI = \frac{P}{PET} \quad (1)$$

308 where P represents precipitation and PET denotes potential evapotranspiration. AI
 309 reflects the balance between atmospheric water supply and evaporative demand.

310 In this study, PET was calculated using the FAO Penman–Monteith method, which
 311 is widely recognized as a physically based and robust approach for estimating

312 atmospheric evaporative demand. PET was computed as:

$$313 \quad PET = \frac{0.408\Delta(R_n - G) + \gamma \frac{900}{T + 273} u_2 (e_s - e_a)}{\Delta + \gamma(1 + 0.34u_2)} \quad (2)$$

314 Where R_n is the net radiation at the surface ($\text{MJ m}^{-2} \text{ day}^{-1}$), G is the soil heat flux
315 ($\text{MJ m}^{-2} \text{ day}^{-1}$), T is the mean air temperature at 2 m height ($^{\circ}\text{C}$), u_2 is the wind speed
316 at 2 m height (m/s), e_s is the saturation vapor pressure (kPa), e_a is the actual vapor
317 pressure (kPa), Δ is the slope of the saturation vapor pressure–temperature curve
318 ($\text{kPa } ^{\circ}\text{C}^{-1}$), and γ is the psychrometric constant ($\text{kPa } ^{\circ}\text{C}^{-1}$).

319 All meteorological variables required for PET estimation were obtained from the
320 ERA5 reanalysis dataset and spatially averaged over the study area to ensure
321 consistency with basin-scale analysis.

322 Based on AI values, climatic conditions were classified following the United
323 Nations Environment Programme (UNEP) scheme: $\text{AI} < 0.05$ indicates hyper-arid
324 conditions, $0.05 \leq \text{AI} < 0.20$ represents arid conditions, $0.20 \leq \text{AI} < 0.50$ corresponds
325 to semi-arid conditions, $0.50 \leq \text{AI} < 0.65$ indicates dry sub-humid conditions, and $\text{AI} \geq$
326 0.65 represents humid conditions. This classification allows a quantitative
327 interpretation of regional aridity and facilitates comparison with previous studies in arid
328 and semi-arid regions.

329 2.2.3 XGBoost Model

330 In this study, the XGBoost model is employed primarily as an interpretative tool.
331 The objective is to quantify the relative importance of different hydro-climatic factors
332 and to explore potential nonlinear relationships between lake-area variability and

333 climatic drivers. Given the limited sample size, strong interannual variability, and high
334 nonlinearity characteristic of arid-region lake systems, model performance metrics (e.g.,
335 R^2) are used as auxiliary indicators, while greater emphasis is placed on feature-
336 importance rankings for mechanism interpretation.

337 Compared with linear correlation analysis, the XGBoost results highlight the
338 importance of nonlinear and season-dependent controls, particularly during transitional
339 seasons when linear correlations are weak. This demonstrates the added value of
340 XGBoost in revealing climatic influences that cannot be fully captured by linear
341 statistical methods alone.

342 The objective function of the XGBoost model is:

$$343 \quad L(\theta) = \sum_{i=1}^n l(y_i, f(x_i)) + \sum_{k=1}^n \Omega(f_k) \quad (3)$$

344 Where $L(\theta)$ represents the objective function, which measures the model's
345 performance in prediction and consists of two parts: $l(y_i, f(x_i))$ is the loss function,
346 indicating the difference between the true value y_i and the predicted value $f(x_i)$,
347 while $\Omega(f_k)$ is the regularization term used to control the model complexity.

348 The input factors $x_i = \{x_1, x_2, \dots, x_n\}$ include precipitation (P), air temperature (T),
349 relative humidity (RH), and potential evapotranspiration (PET), which represent the
350 primary components of the lake water balance in arid and semi-arid regions. These
351 variables directly or indirectly regulate lake-area changes through their influence on
352 water input and evaporative loss. Energy-related variables (e.g., radiation and heat
353 fluxes) are included as background indicators of atmospheric conditions and are not
354 interpreted as direct driving forces of lake-area change.

355
$$FI(x_j) = \frac{1}{T} \sum_{t=1}^T I(t, x_j) \quad (4)$$

356 Here, $FI(x_j)$ represents the feature importance of factor x_j , while $I(t, x_j)$
 357 denotes the contribution of factor x_j when used as a splitting point in tree t , with T
 358 being the total number of trees. The generated feature importance ranking chart
 359 illustrates the contribution of various input factors (such as temperature, precipitation,
 360 and humidity) to lake area changes. This ranking chart provides an intuitive way to
 361 identify the most influential factors.

362 To improve model performance, hyperparameters can be optimized using Grid
 363 Search or Random Search. Common hyperparameters include Learning rate, Max depth
 364 of trees and Number of trees. Adjusting these parameters affects the model's fitting
 365 ability and generalization performance.

366 Data Splitting: Divide the dataset into a training set and a test set (e.g., 80% for
 367 training, 20% for testing).

368 Train the XGBoost model on the training set. XGBoost uses the Gradient Boosting
 369 Algorithm, which iteratively improves the model by building multiple weak learners to
 370 reduce prediction errors. Each iteration refines the model by fitting the residuals (i.e.,
 371 prediction errors).

372 Model Validation: Evaluate model performance using metrics such as Mean
 373 Squared Error (MSE) and Coefficient of Determination (R^2) to assess accuracy and
 374 stability.

375 The formula for Mean Squared Error (MSE) is:

376
$$MSE = \frac{1}{n} \sum_{i=1}^n (y_i - f(x_i))^2 \quad (5)$$

377 The formula for the coefficient of determination R^2 is:

$$378 \quad R^2 = 1 - \frac{\sum_{i=1}^n (y_i - f(x_i))^2}{\sum_{i=1}^n (y_i - \bar{y})^2} \quad (6)$$

379 Where \bar{y} represents the mean of the samples.

380 The lake area model is based on model training, the predicted lake area \hat{y} can be
381 expressed as a nonlinear combination of input factors x_i :

$$382 \quad \hat{y} = f(x_i) = \sum_{k=1}^K \omega_k h_k(x_i) \quad (7)$$

383 Where: ω_k is the weight of the k tree, and $h_k(x_i)$ is the prediction function of the
384 tree, represented as a set of decision rules.

385 The feature importance derived from the XGBoost model reflects the relative
386 contribution of each climatic variable in reducing prediction error across all decision
387 trees. It should be noted that this importance ranking does not imply direct causality,
388 but rather indicates the sensitivity of lake-area variability to different climatic factors
389 under nonlinear interactions. Therefore, feature importance is interpreted in conjunction
390 with linear correlation analysis to provide a more robust understanding of hydro-
391 climatic controls.

392 **3. Lake area time series construction**

393 **3.1 Remote sensing interpretation and monthly lake image synthesis**

394 3.1.1 Selection of water indices and image preprocessing

395 The study area is located in a high-altitude region, where lake surfaces freeze
396 between November and March. Since the NDWI index is less effective for frozen lakes,

397 different indices are used for different seasons. During the non-freezing period (May–
398 November), the NDWI index is applied for conventional water body extraction. During
399 the freezing period (December–April), the Modified Normalized Difference Snow
400 Index (MNDSI) is used to evaluate water surface area.

401 The NDWI index utilizes the strong absorption of water bodies in the near-infrared
402 band and their high reflectance in the green band to enhance the distinction between
403 water and other land cover types. However, this index may misidentify bright white
404 buildings, clouds, snow, and mountain shadows as water bodies. Therefore, additional
405 data quality bands and methods are integrated to remove these interferences and
406 improve the accuracy of water body extraction.

$$407 \quad NDWI = \frac{(Green - NIR)}{(Green + NIR)} \quad (8)$$

408 Where: Green band typically refers to the green portion of the visible spectrum,
409 generally ranging from 500–570 nm. NIR band refers to the near-infrared spectrum,
410 generally ranging from 800–900 nm.

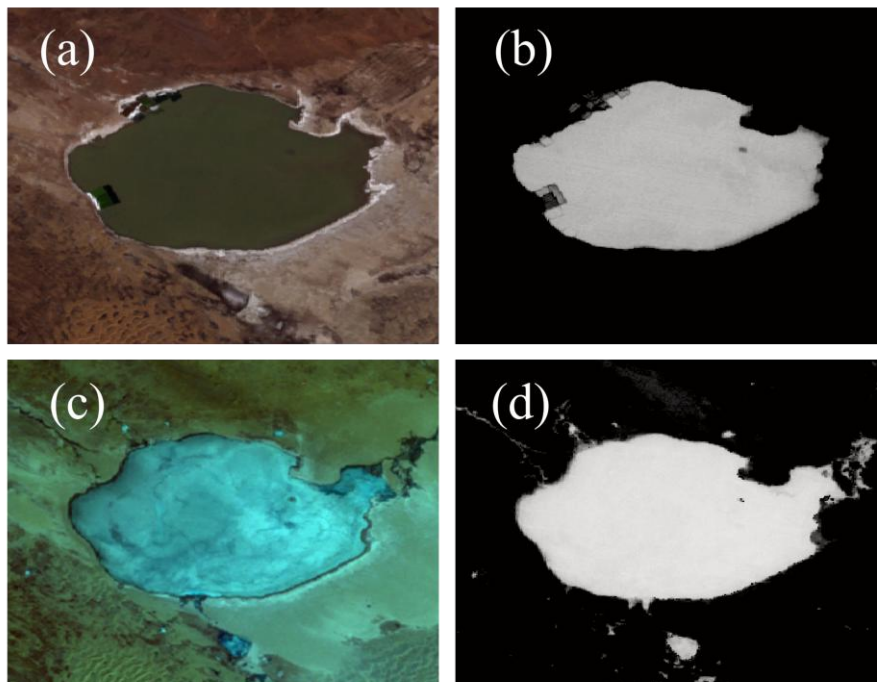
411 The Modified Normalized Difference Snow Index (MNDSI) is an index calculated
412 using the reflectance of the near-infrared (NIR) and short-wave infrared (SWIR) bands.
413 It is an effective method for distinguishing ice surfaces from water bodies. This index
414 is particularly suitable for regions with frozen water surfaces, such as lakes and rivers,
415 where seasonal changes are significant. Ice surfaces and water bodies have different
416 reflectance characteristics in various bands. Ice has higher reflectance in the SWIR band,
417 while water has lower reflectance. By calculating the difference between the NIR and
418 SWIR bands, MNDSI can effectively distinguish between ice surfaces and water bodies,

419 thus improving the accuracy of ice extraction. By combining these two bands, MNDSI
420 highlights the differences between water bodies and ice surfaces, making it easier to
421 differentiate between them. Similar to NDWI, MNDSI enhances the contrast between
422 ice and water by utilizing reflectance values from different bands.

423 MNDSI (Modified Normalized Difference Snow Index) is calculated by
424 combining the reflectance of the near-infrared (NIR) and short-wave infrared (SWIR)
425 bands. The typical formula for MNDSI is as follows:

$$426 \quad MNDSI = \frac{NIR - SWIR}{NIR + SWIR} \quad (9)$$

427 Where NIR is the reflectance in the near-infrared band (typically 800–900 nm),
428 SWIR is the reflectance in the short-wave infrared band (typically 1500–1700 nm).



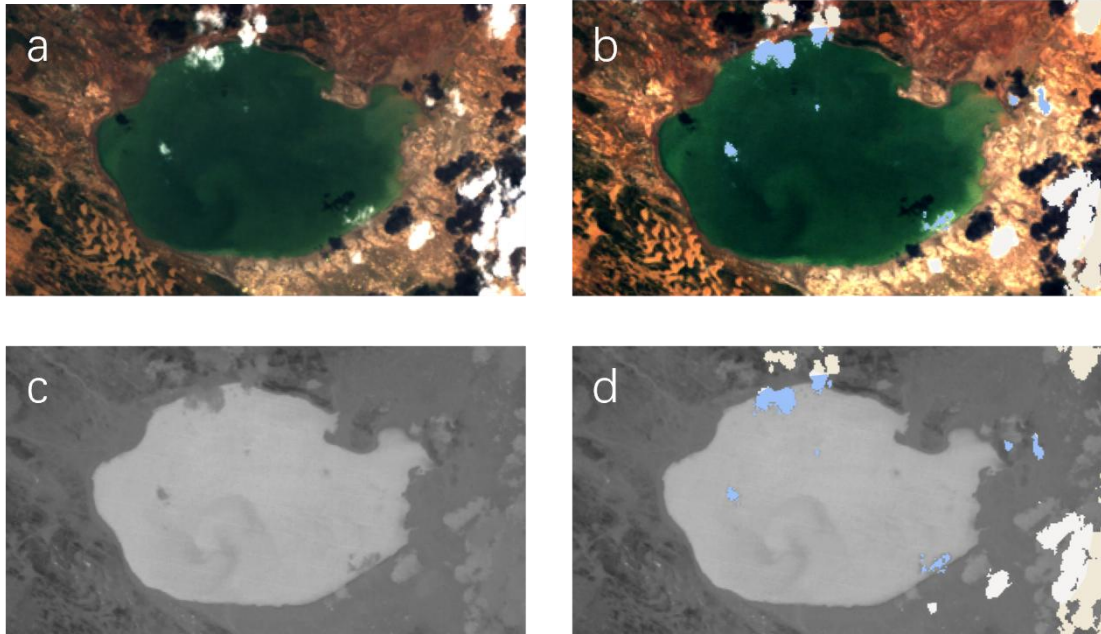
429
430 Figure 3 Lake extraction from Landsat imagery during non-freezing and freezing periods. (a)
431 Original Landsat image during the non-freezing period;(b) Lake area identified using NDWI;(c)
432 Original Landsat image during the freezing period;(d) Lake area identified using MNDSI. Source:

433 Landsat imagery courtesy of the U.S. Geological Survey (USGS), processed and interpreted by the
434 authors.

435 The cloud and snow interference removal is only applied to the NDWI of the non-
436 freezing period from May to November. The Landsat series satellites provide their own
437 pixel-scale data quality band (QA_PIXEL), which can be used to eliminate noise pixels
438 in the image.

439 The QA_PIXEL band in the Landsat dataset provides information on various
440 quality types, where different bits (Bit) correspond to different types of quality
441 information. For example, Bit 3 corresponds to clouds, Bit 5 corresponds to snow, and
442 Bit 7 corresponds to water bodies. Within the same bit, values of 0 and 1 represent
443 different data qualities. For example, a 0 in Bit 7 indicates that the pixel has poor water
444 body information, being land or covered by clouds, while a 1 indicates that the pixel
445 represents water.

446 Using this pixel quality information, we selected Bit 3 (cloud), Bit 5 (snow), and
447 Bit 7 (water body). By performing bitwise AND and OR operations, we generated a
448 water body mask file with good data quality after cloud and snow removal. This mask
449 file is then overlaid with the actual image to remove pixels affected by cloud or snow
450 interference. The effect of cloud and snow removal is shown in the image below:



451

452

Figure 4. Illustration of cloud and snow removal and its effect on NDWI-based water extraction.

453

(a) True-color Landsat image before cloud and snow removal. (b) True-color image after cloud and

454

snow masking, where contaminated pixels are excluded. (c) NDWI image derived from the original

455

true-color image, shown in grayscale, with brighter values indicating higher likelihood of water

456

presence. (d) NDWI image after cloud and snow removal; blue areas indicate pixels affected by

457

cloud or snow that were excluded from water-body extraction. Source: Landsat imagery courtesy of

458

the U.S. Geological Survey (USGS), processed and interpreted by the authors.

459

The NDWI, MNDSI index calculation, and cloud/snow interference removal are

460

performed directly on the GEE platform, followed by monthly composite image

461

downloads. Based on the cloud cover information ('CLOUD_COVER'), which

462

represents the cloud amount (range from 0 to 100, with larger values indicating more

463

cloud coverage), the data is classified into three levels: 0-30, 30-60, and 60-100. If data

464

is available in Level 1, Level 2 is not executed, and if Level 2 contains data, Level 3 is

465

processed. All images from each year and month within the cloud cover level are

466 selected, and the median pixel value is calculated to generate the composite monthly
467 NDWI (for 5-11 months) and MNDSI (for December to the following April) grayscale
468 images.

469 Data is filtered based on the cloud cover proportion C , where $C \in [0,100]$.

470 Composite image=Med($S(C)$), where $C=CLOUD_{COVER}$

$$471 \quad S(C) = \begin{cases} I(C) & \text{if } 0 \leq C \leq 30 \\ I(C) & \text{else if } 30 < C < 60 \\ I(C) & \text{else } 60 < C \leq 100 \end{cases} \quad (10)$$

472 Where $I(C)$ is a set of image data filtered by cloud cover.

473 3.1.2 Threshold-based water segmentation and noise removal

474 Lake water pixels were first identified using threshold-based segmentation. To
475 reduce false positives caused by mountain shadows and built-up areas, topographic and
476 ancillary data were applied to remove non-water pixels.

477 (1) Threshold segmentation

478 This step applies the Otsu threshold algorithm to the downloaded NDWI and
479 MNDSI monthly composite grayscale images, automatically generating a segmentation
480 threshold. Pixels below the threshold are classified as water, and those above the
481 threshold are classified as other areas.

482 The core of the Otsu thresholding method is to divide the image into two classes
483 (foreground and background) by maximizing the between-class variance, thereby
484 achieving the optimal threshold segmentation. Specifically, it involves iterating through
485 all possible thresholds, and the optimal threshold is determined when the between-class
486 variance is maximized while the variance within both the foreground and background

487 is minimized. Compared to other methods, this algorithm maximizes the inclusion of
488 the target feature while excluding other interfering factors.

489 The Otsu thresholding method is used to automatically generate the segmentation
490 threshold, dividing the image into water and other regions:

$$491 \quad T = \arg \max_{\tau} \max(\sigma_B^2(\tau)) \quad (11)$$

492 Where, $\sigma_B^2(\tau)$ is the between-class variance, defined as:

$$493 \quad \sigma_B^2(\tau) = \omega_1(\tau)\omega_2(\tau)(\mu_1(\tau) - \mu_2(\tau))^2 \quad (12)$$

494 Where $\omega_1(\tau)$ and $\omega_2(\tau)$ are the weights of the foreground and background at
495 the threshold τ , and $\mu_1(\tau)$ and $\mu_2(\tau)$ are the mean gray values of the foreground and
496 background, respectively.

497 The portion smaller than the threshold T is classified as water, symbolized as water
498 pixels, while the portion greater than the threshold is classified as other categories.

499 (2) Mountain shadow and buildings removal

500 Since the lake surface typically exhibits a flat state without significant slope and
501 aspect features, digital elevation models (DEM) can be used to distinguish lakes from
502 mountainous regions by utilizing slope and aspect information. By setting threshold
503 values of 0 for slope and aspect, the distinction between lakes and mountainous areas
504 can be made. However, the current frequency of elevation data updates does not align
505 with real-time imagery, leading to an inability to accurately reflect seasonal changes in
506 lake water levels within the elevation data. This limitation affects the precision of water
507 body area extraction using the data. Given that most lakes are interconnected, this study
508 employs the maximum connected component analysis algorithm from the Open-CV

509 vision field to define the boundaries of lakes and extract their areas.

510 By setting the thresholds for slope θ and aspect ϕ to 0 in the digital elevation model
511 (DEM), lakes are distinguished from mountainous areas:

$$512 \quad \theta(x, y) = 0, \quad \phi(x, y) = 0 \quad (13)$$

513 Where $\theta(x, y)$ and $\phi(x, y)$ represent the slope and aspect values at a given
514 point (x, y) , respectively. By setting $\theta(x, y) = 0$ and $\phi(x, y) = 0$ as threshold
515 conditions for the lake area, the lake region is defined as the area where both the slope
516 and aspect are equal to 0.

$$517 \quad L = \max_i \left(\sum_{(x,y) \in C_i} I(x, y) \right) \quad (14)$$

518 Where L represents the total number of pixels in the largest lake area, C_i
519 represents the i -th connected component in the image, the function \sum denotes the
520 summation of pixel points, and \max_i indicates the selection of the largest connected
521 component as the lake area.

522 The construction of the building index currently mainly relies on the fact that the
523 surface temperature of buildings is usually higher than that of surrounding land cover,
524 and the mid-infrared band can effectively reflect surface temperature differences.
525 However, in previous land cover classification studies, the extraction results using this
526 algorithm were not ideal. Considering that most buildings in the study area are not
527 distributed along lakes, the maximum connected component algorithm can effectively
528 exclude parts where buildings are misidentified as water bodies.

529 Based on the NDWI (Normalized Difference Water Index), a threshold T is used

530 to binarize the image, separating water bodies from non-water bodies.

$$531 \quad I(x, y) = \begin{cases} 1, & \text{if } NDVI(x, y) > T \\ 0, & \text{if } NDVI(x, y) \leq T \end{cases} \quad (15)$$

532 Connected Component Calculation: In the binarized image, the Connected
533 Components Labeling (CCL) algorithm is used to identify all connected regions. A
534 connected component is determined by scanning the neighboring pixels in the image
535 (up, down, left, right, or diagonally). The formula is expressed as:

$$536 \quad C_i = \sum_{(x,y) \in R} I(x, y) \quad (16)$$

537 Where R represents the connected regions in the image, and C_i denotes the
538 connected components.

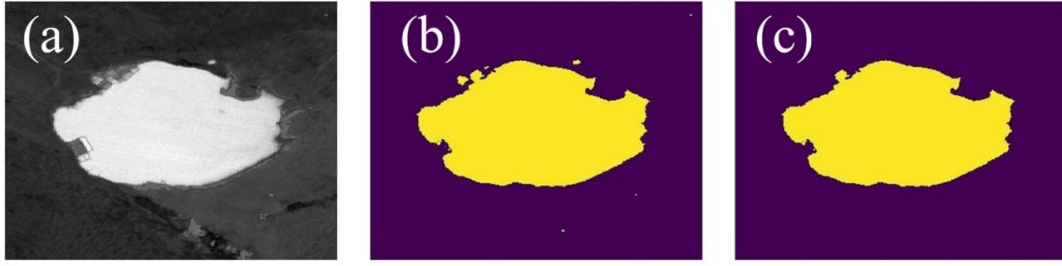
539 To eliminate interference from buildings, a threshold condition τ is set, retaining
540 only connected components with an area greater than τ . Since buildings typically have
541 smaller areas, while lakes exhibit larger connected components, the lake regions can be
542 filtered using the following condition:

$$543 \quad C_i > \tau \quad (17)$$

544 The lake boundary is extracted using a boundary detection algorithm (e.g., the
545 Canny edge detection algorithm) applied to the selected largest connected region.

$$546 \quad B = \text{Canny}(C_i) \quad (18)$$

547 As shown in the Figure 5, the white areas in the original image include both lakes
548 and buildings. When using threshold segmentation to extract water bodies, buildings
549 may also be mistakenly identified as water. By applying the maximum connected
550 component method, buildings can be effectively separated.



551

552

Figure 5. Illustration of water extraction and building removal processes. (a) Original Landsat

553

image, in which white areas include both lake water and built-up surfaces; (b) water bodies extracted

554

using threshold-based segmentation; (c) buildings separated from water bodies using the maximum

555

connected component method. Source: Landsat imagery courtesy of the U.S. Geological Survey

556

(USGS), processed and interpreted by the authors.

557

3.1.3 Cloudy and striped image reconstruction

558

(1) Cloudy image filling processing

559

For cloud-free images, the subsequent water-extraction steps are applied directly.

560

For cloudy images, cloud-free images are first used to reconstruct missing pixels, after

561

which the same processing steps are executed.

562

The filling approach is as follows: Based on the cloud coverage information

563

($CLOUD_COVER$), images with cloud cover less than or equal to 30%

564

($CLOUD_COVER \leq 30\%$) are classified as cloud-free images, while others are

565

considered cloudy images. The formula is as follows:

566

$$\begin{aligned} \text{Cloudy Image} &= \{\text{Image} \mid CLOUD_{COVER} \leq 30\%\} \\ \text{Cloud-Free Image} &= \{\text{Image} \mid CLOUD_{COVER} > 30\%\} \end{aligned} \quad (19)$$

567

Then, the Mutual Information (MI) algorithm is used to perform the most similar

568

matching between the cloudy image and all cloud-free images. Next, the most similar

569

image is combined with the original cloudy image through a union operation to obtain

570 the filled cloudy image. Finally, the reconstructed images are processed using the same
571 lake-extraction workflow as applied to cloud-free images, producing the final water-
572 body area estimates:

573 Candidate Cloud-Free Image Set: In the time periods before and after the cloudy
574 image, select images with low cloud coverage ($\text{CLOUD_COVER} \leq 30\%$) as the
575 candidate image set.

576 Mutual Information Algorithm: Use the MI algorithm to calculate the similarity
577 between the cloudy image and the candidate cloud-free images. The formula is as
578 follows:

$$579 \quad I(I_{cloudy}, I_{clear}) = \sum_{i,j} p(I_{cloudy} = i, I_{clear} = j) \log \left(\frac{p(I_{cloudy} = i, I_{clear} = j)}{p(I_{cloudy} = i) p(I_{clear} = j)} \right) \quad (20)$$

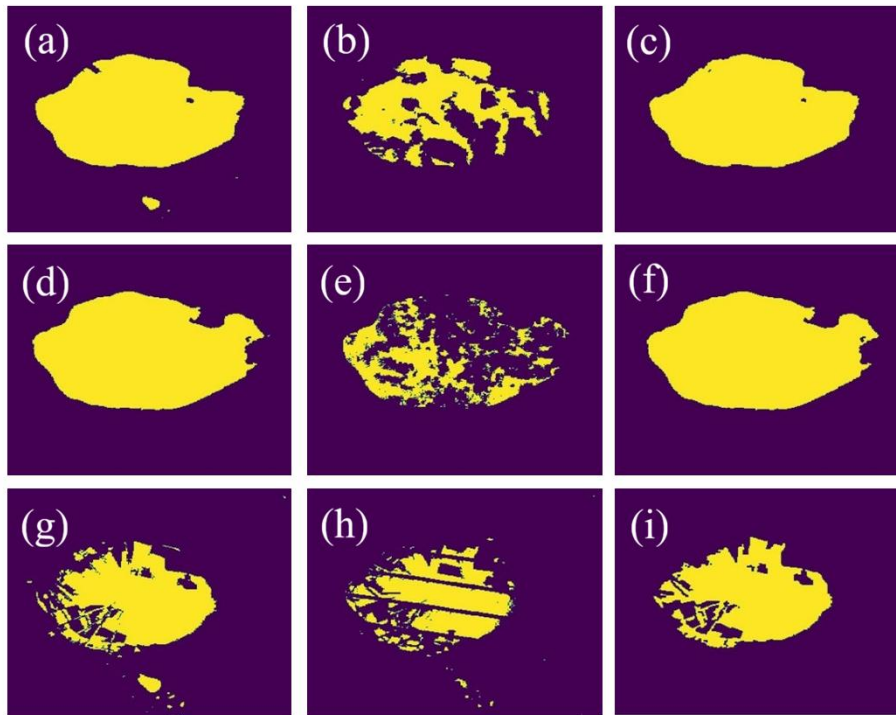
580 Where I_{cloudy} represents the cloudy image, I_{clear} represents the candidate cloud-
581 free image, and p is the joint probability distribution of the pixel grayscale values. I
582 denotes mutual information, which measures the correlation between the cloudy image
583 and the cloud-free image.

584 Selecting the Most Similar Image: Based on the mutual information value, the
585 cloud-free image most similar to the cloudy image is selected.

586 (2) Striped image filling

587 The previously mentioned dataset indicates that Landsat 7 TM images have
588 significant striping interference. Additionally, Landsat 5 TM and Landsat 8 OLI images
589 also experience striping interference in certain months, such as Landsat 5 TM from
590 2001 to 2003 and Landsat 8 in 2008. To more accurately obtain the temporal changes
591 in lake area, it is necessary to fill the missing portions of striped images. The method is

592 the same as for cloud-filled images. By utilizing the clear contours of historical cloud-
593 free images and applying the MI algorithm, the most similar historical cloud-free
594 images are searched to fill the water pixels in the striped regions. The method for filling
595 striped images is the same as that for cloud-filled images.



597 Figure 6: Filling processing of cloudy and striped-interference lake images using similar cloud-
598 free references. (a)\(d) Cloud-free reference images identified as most similar to the cloudy images;
599 (b)\(e) Original cloudy images;(c)\(f) Cloud-filled results after processing; (g) Cloud-free image
600 most similar to the striped-interference image;(h) Original striped-interference image;(i) Result after
601 stripe-filling processing. Source: Landsat imagery courtesy of the U.S. Geological Survey (USGS),
602 processed and interpreted by the authors.

603 3.1.4 Monthly synthesis and time-series construction

604 After applying the maximum connectivity component processing to the image, the
605 number of water pixels is counted. Then, based on the spatial resolution of the pixels

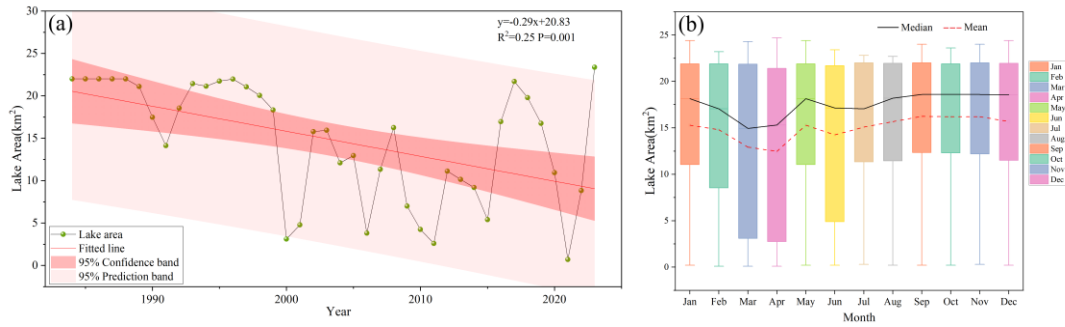
606 (30m * 30m), the actual area is calculated.

607 Collect all known lake area data for specific time points, where t_i dots represent
608 time points with available data. For each missing data point t_{missing} , use the known data
609 points $t_{\text{missing}-1}$ and $t_{\text{missing}+1}$, and apply the selected interpolation method to calculate
610 the lake area $A(t_{\text{missing}})$ at time.

611 **3.2 Lake area time series construction**

612 3.2.1 Monthly lake-area time series and seasonal variability of Bahannao Lake

613 The interannual variation of Bahannao is quite drastic, but the overall trend is
614 declining (Figure 7(a)), linear regression analysis based on the year index reveals a
615 significant declining trend in the lake area from 1984 to 2024, with a decrease rate of
616 $-0.29 \text{ km}^2 \text{ yr}^{-1}$ ($p = 0.001$). The coefficient of determination ($R^2 = 0.25$) indicates
617 substantial interannual variability, suggesting that although the long-term trend is
618 statistically robust, short-term fluctuations and nonlinear processes play an important
619 role in shaping lake-area dynamics. Before 1999, the changes were relatively stable. In
620 2000, the lake area shrank severely, decreasing by 82.98% compared to 1999, leaving
621 only 3.12 km². Since then, the lake has exhibited a cyclical fluctuation pattern with a
622 period of approximately 5–6 years. In 2021, the lake area reached its minimum value
623 of just 0.71 km², followed by a rapid increase, reaching its maximum of 23.38 km² in
624 2023.



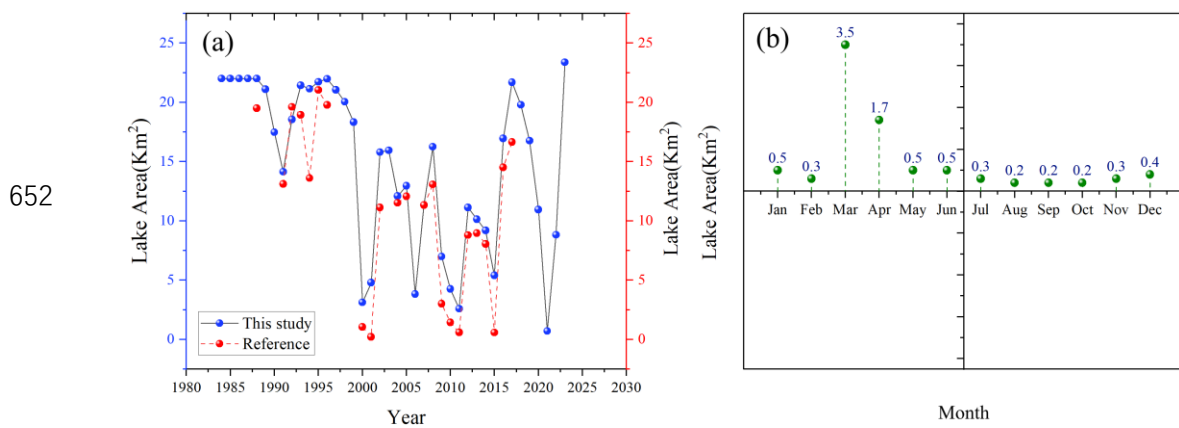
625
626 Figure 7 Interannual and intra-annual variation of Bahannao Lake area. (a) Interannual
627 variations of lake area; (b) multi-year mean monthly variations of lake area.

628 Due to its location in the Mu Us Desert and the lack of long-term observational
629 data, this study references the lake area interpreted via remote sensing in the
630 *Comprehensive Lake Water Ecological Management Plan of Uxin Banner*. This report
631 provides remote sensing imagery data for 24 years from 1988 to 2018 (with six years
632 lacking clear images suitable for analysis).

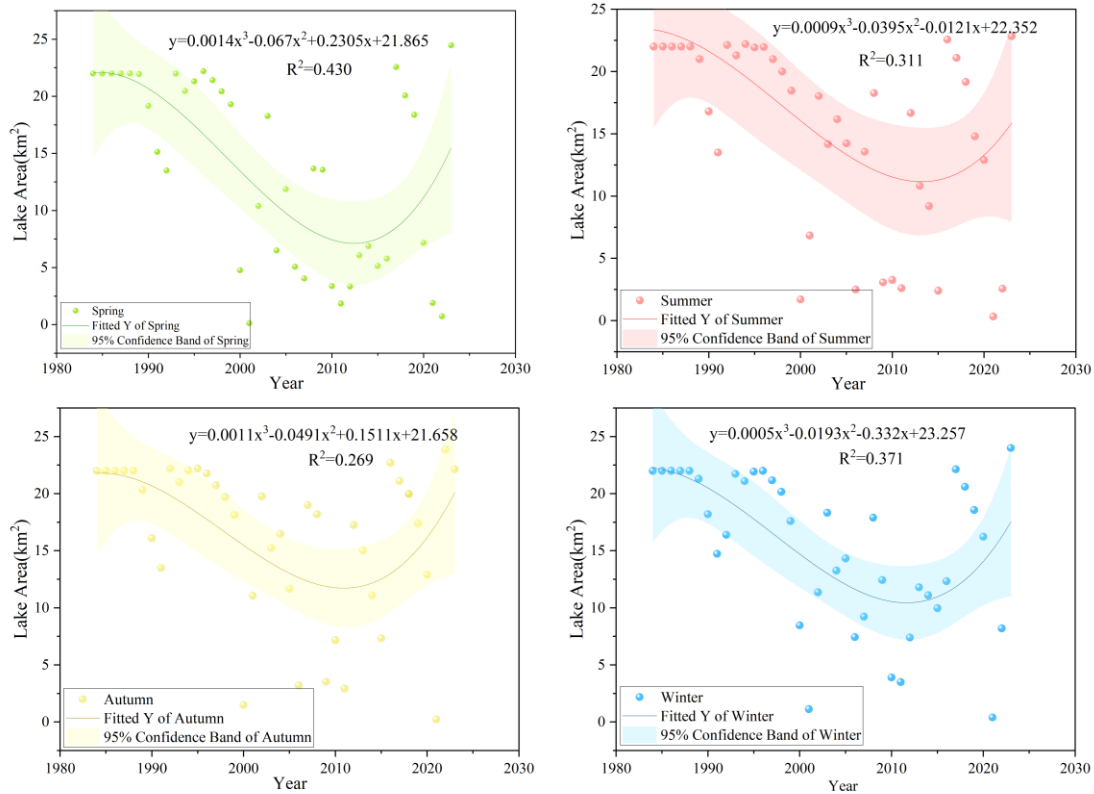
633 A comparison of the data (Figure 8(a)) shows that the lake area interpreted in this
634 study aligns with the trend reported in the management plan. Over the 23 years of
635 overlapping interpretation, the error remains within 15% for 12 years. However, in
636 years when the lake area was smaller, the error was relatively larger, such as in 2000,
637 2001, 2009, 2010, 2011, and 2015. According to records, Bahannao Lake shrank
638 significantly during these years but did not completely dry up until 2021, which is
639 consistent with the results of this study.

640 The interpreted lake area in this study also indicates (Figure 8(b)) that the annual
641 average area of Bahannao Lake in 2021 was only 0.71 km². The lake area was at its
642 smallest in August, September, and October, reaching only 0.2 km², while the largest
643 area was recorded in March at 3.5 km². The rapid expansion of the lake area observed

644 in the spring of 2021 may be related to short-term hydrological inputs. Although the
 645 precipitation in this region during winter and early spring is generally limited,
 646 occasional short-term precipitation events or snowmelt may temporarily increase
 647 surface runoff and inflow to the lake. In addition, as temperatures rise in late spring,
 648 enhanced evaporation and reduced inflow may lead to a rapid decrease in lake area.
 649 Therefore, the rapid increase and subsequent decrease in lake area in spring 2021 may
 650 reflect the combined effects of short-term hydrological inputs and seasonal evaporation
 651 processes.



653 Figure 8 Validation of lake area estimates and intra-annual variability in a typical year (2021).
 654 (a) Comparison between lake area derived in this study and reference datasets;(b) monthly variations
 655 of lake area in 2021, selected as a representative year to illustrate intra-annual dynamics.



656

657

Figure 9 Seasonal variation of lake area during the period of 1984-2024

658

From the perspective of seasonal (Figure 9) and monthly (Figure 7(b)) variation characteristics, Bahannao exhibits significant seasonal differences. The lake area in summer, autumn, and winter is noticeably larger than in spring, with autumn having the largest lake area, averaging 16.21 square kilometers and reaching a peak of 16.24 square kilometers in September. In contrast, spring has the smallest lake area, averaging only 13.57 square kilometers, with the lowest value of 12.48 square kilometers occurring in April.

664

665

3.2.2 Method validation using representative lakes in arid regions

666

667

668

To further evaluate the robustness and regional applicability of the proposed lake-area extraction method, we applied the same remote-sensing workflow to two representative lakes in arid and semi-arid northern China: Hongjiannao Lake and

669 Wuliangshuai Lake. These lakes differ markedly in size, hydrological conditions, and
670 degree of human influence, and have been widely investigated in previous remote-
671 sensing studies, providing independent reference datasets for method validation.

672 Using the identical image-processing procedures and water-body extraction
673 criteria as those employed for Bahannao Lake, we constructed annual lake-area time
674 series for both Hongjiannao Lake and Wuliangshuai Lake (Figure 10). The derived time
675 series capture the major interannual fluctuations and long-term trends of lake-area
676 variability for both lakes.

677 To quantitatively assess consistency with existing studies, the lake-area estimates
678 obtained in this study were compared with previously published lake-area datasets
679 (Figure 11). For both lakes, the temporal evolution and long-term trends derived in this
680 study show good agreement with reference datasets reported in the literature.

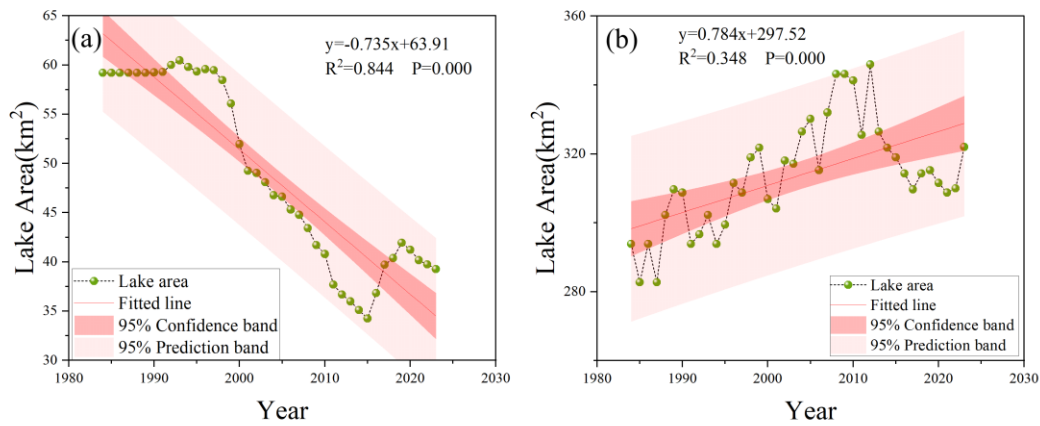
681 For Hongjiannao Lake, quantitative comparison indicates that the relative
682 differences between lake-area estimates derived in this study and published datasets
683 generally remain within a reasonable range. Specifically, the maximum and minimum
684 relative differences are 14.65% and 9.12% when compared with Ji et al. (2023), 18.70%
685 and 9.57% with Xie et al. (2021), 11.82% and 8.29% with Ma et al. (2020), 11.30% and
686 7.94% with Wang et al. (2018), and 10.57% and 3.15% with Liu et al. (2016).

687 For Wuliangshuai Lake, the relative differences are generally smaller, with
688 maximum differences of 8.50% (minimum 1.74%) compared with Guan et al. (2022),
689 8.02% (minimum 1.79%) compared with Li et al. (2023), and 18.12% (minimum 1.09%)
690 compared with Tan et al. (2021). These results indicate a high level of consistency

691 between the lake-area estimates derived in this study and those reported in previous
692 literature.

693 Although minor discrepancies in absolute lake-area values are observed, these
694 differences can be attributed to variations in image selection, water-index thresholds,
695 temporal coverage, and post-processing strategies among different studies. An
696 additional source of discrepancy arises from differences in temporal aggregation
697 strategies. In this study, annual lake area is calculated as the mean of monthly lake-area
698 estimates derived from all available images within a year, which reduces the influence
699 of short-term fluctuations and image-specific noise. In contrast, many previous studies
700 report lake area based on a single image or a limited number of images selected for each
701 year. Such differences in temporal representation can lead to systematic deviations in
702 absolute lake-area values, particularly for lakes exhibiting strong intra-annual
703 variability.

704 Overall, the consistency between our results and independent reference datasets
705 supports the robustness and transferability of the proposed lake-area extraction method
706 across different lake types in arid and semi-arid regions. This validation provides
707 confidence that the method is suitable for long-term lake-area monitoring and
708 comparative analysis in data-sparse dryland environments.



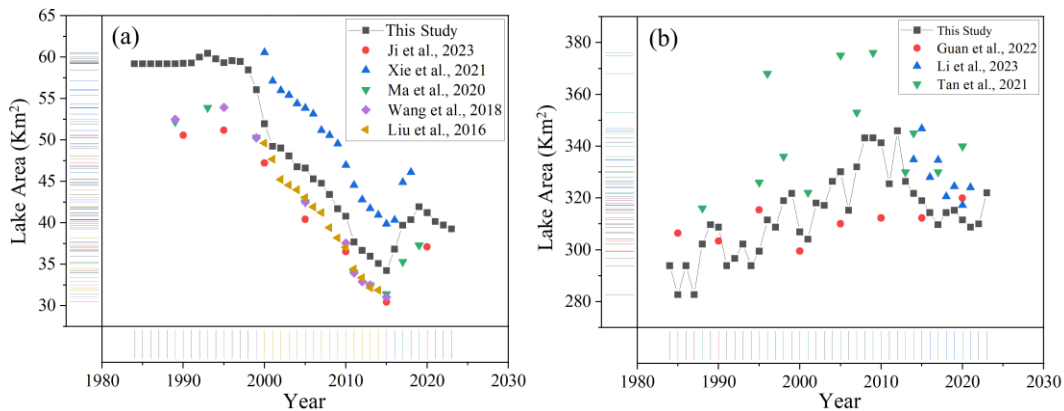
709

710

Figure 10 Interannual variations in lake area for Hongjiannao Lake (a) and Wuliangshuhai Lake

711

(b).



712

713

Figure 11 Comparison of lake area estimates derived in this study with published reference

714

datasets. (a) Comparison of Hongjiannao Lake area with lake-area estimates reported in previous

715

studies; (b) Comparison of Wuliangshuhai Lake area with lake-area estimates reported in previous

716

studies.

717

3.3 Impact of climate change

718

3.3.1 Changes of hydro-climate series

719

(1) Temperature and moisture conditions

720

1) Temperature and 2m dew point temperature

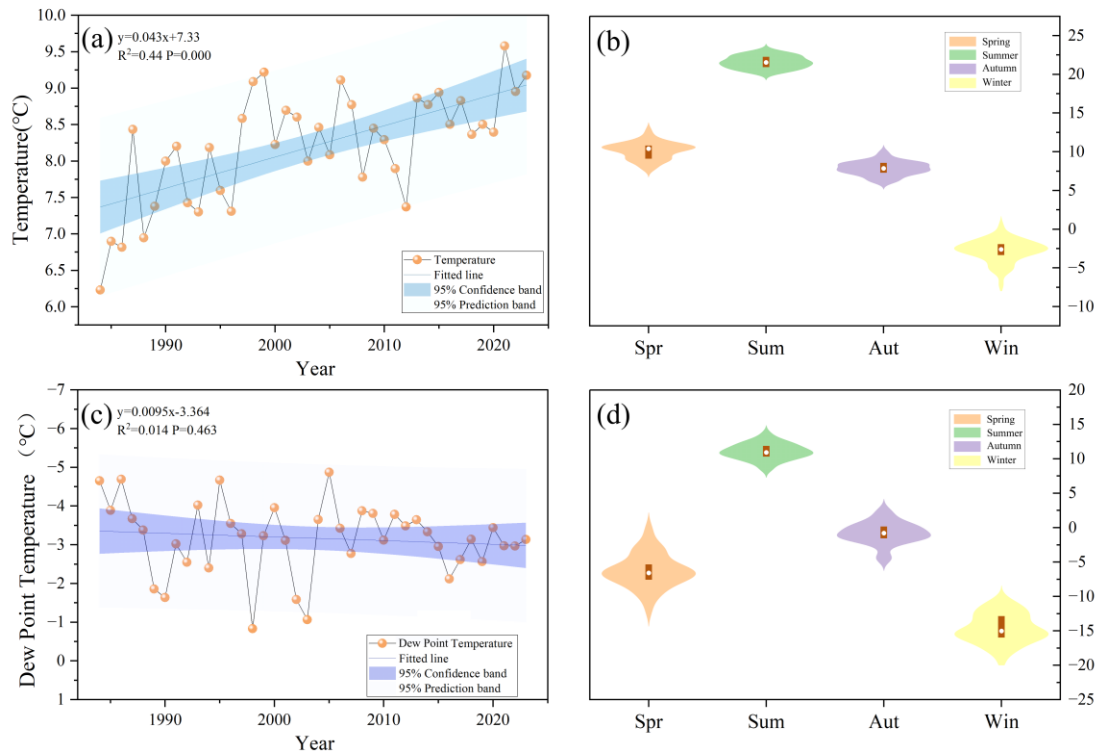
721

The rise in air temperature directly affects the evaporation rate of the lake. The

722 warming rate is $0.043^{\circ}\text{C yr}^{-1}$ (Figure 12(a)), leading to an increase in the lake surface
723 temperature and, consequently, higher evaporation. High temperatures intensify water
724 evaporation, reducing the lake's water volume and causing a gradual decrease in lake
725 area over the years.

726 The increase in air temperature enhances heat input into the water body,
727 accelerating evaporation. As more heat is absorbed, surface water transforms more
728 easily into water vapor, leading to a decline in lake water levels. Although the influence
729 of temperature on lake area varies across different time periods, its continuous upward
730 trend has a long-term impact on the reduction of lake area.

731 The 2m dew point temperature increases at a rate of $0.0095^{\circ}\text{C yr}^{-1}$ (Figure 12(c)),
732 indicating changes in atmospheric humidity. A rising dew point temperature suggests
733 an increase in water vapor content in the air, typically associated with higher humidity.
734 However, humidity changes do not always directly impact lake area; instead, they
735 influence lake water volume indirectly by affecting evaporation and precipitation.
736 While an increase in dew point temperature usually indicates higher humidity, if
737 precipitation is insufficient or evaporation rates are too high, this increase in humidity
738 may not effectively replenish lake water. Instead, it could contribute to lake shrinkage.
739 The varying influence of the 2m dew point temperature over different periods suggests
740 a complex relationship with lake area changes, requiring a comprehensive analysis
741 alongside other climatic factors.



742

743

Figure 12 Temporal and seasonal variations in air temperature and 2 m dew point temperature

744

over the study area during the period of 1984-2024 ((a) Interannual variations in air temperature; (b)

745

Multi-year mean seasonal cycle of air temperature;(c) Interannual variations in 2 m dew point

746

temperature;(d) Multi-year mean seasonal cycle of 2 m dew point temperature)

747

2) Precipitation and relative humidity

748

The total precipitation is decreasing at a rate of 1.736 mm yr^{-1} (Figure 13(a)).

749

Precipitation is one of the primary sources of lake water. A reduction in precipitation

750

leads to insufficient water replenishment for the lake, resulting in a decline in water

751

levels and a reduction in lake area.

752

The relative humidity decreases at a rate of 0.099 yr^{-1} (Figure 13(c)). A decrease

753

in humidity typically accelerates evaporation from the lake, leading to a reduction in

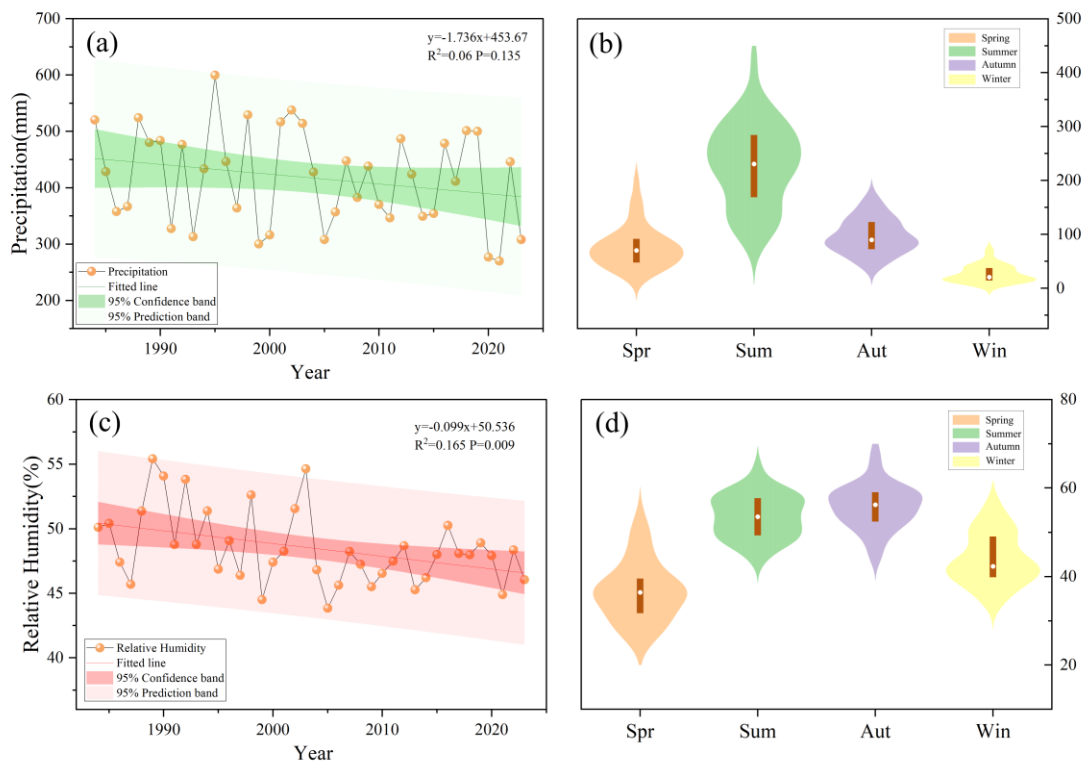
754

lake area. The decrease in humidity means that the air becomes drier, and the

755

evaporation rate increases. This accelerates the evaporation of lake water, resulting in

756 a decline in both lake water levels and area, intensifying the process of lake desiccation.



757

758 Figure 13 Temporal and seasonal variations in precipitation and relative humidity over the
759 study area during the period of 1984-2024 ((a) Interannual variations in precipitation; (b) Multi-year
760 mean seasonal cycle of precipitation;(c) Interannual variations in relative humidity;(d) Multi-year
761 mean seasonal cycle of relative humidity)

762 (2) Surface radiation and heat flux components

763 1) Net longwave radiation and net shortwave radiation at the surface

764 Net longwave radiation at the surface decreases by $0.084 \text{ W/m}^2 \text{ yr}^{-1}$ (Figure 14(a)).

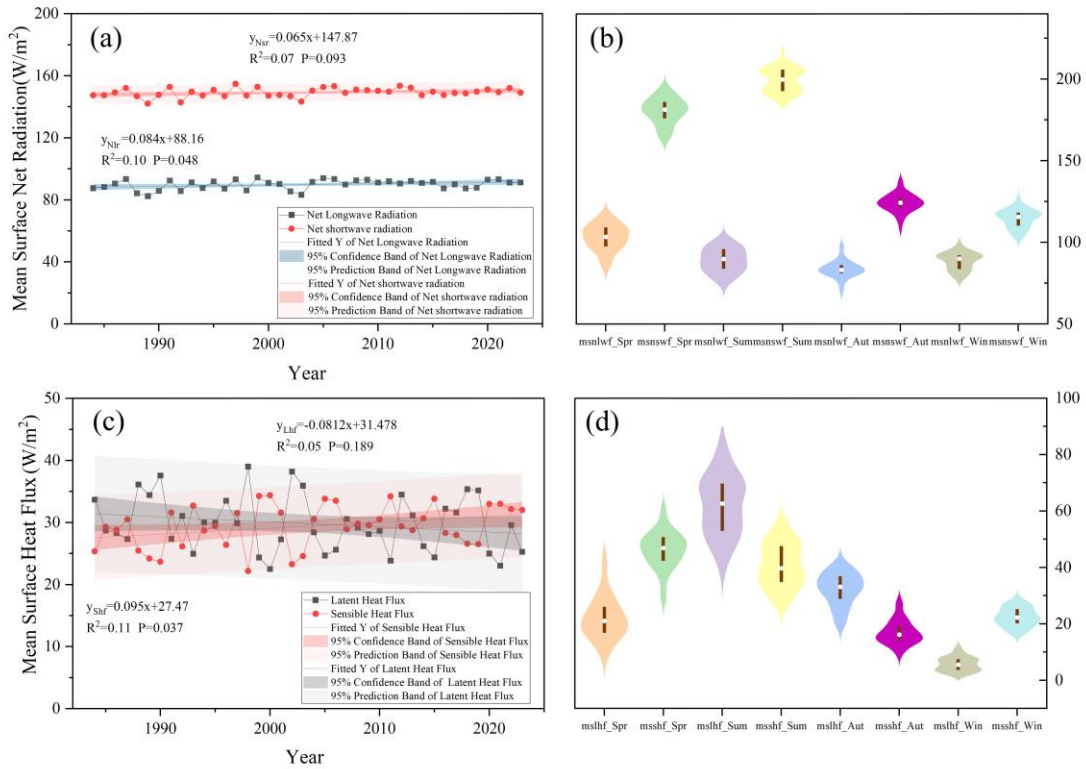
765 The reduction in longwave radiation means that the lake receives less radiative heat,
766 which theoretically could reduce evaporation. However, this effect is overshadowed by
767 other factors such as reduced precipitation and rising temperatures. While the decrease
768 in longwave radiation could reduce heat loss from the lake, in conditions of drought
769 and high evaporation, the impact of this reduction is likely limited.

770 Net shortwave radiation at the surface increases by $0.065 \text{ W/m}^2 \text{ yr}^{-1}$ (Figure 14(a)).
771 The increase in shortwave radiation enhances the evaporation process, thereby reducing
772 the lake's surface area. The rise in shortwave radiation leads to an increase in surface
773 temperature, which accelerates evaporation. The intensified evaporation exacerbates
774 the loss of water from the lake. The effect of increased shortwave radiation on the lake's
775 area is significant during all periods, especially under drought and high-temperature
776 conditions, where its impact is particularly pronounced.

777 2) Mean surface latent heat flux and sensible heat flux

778 The latent heat flux decreases at a rate of $0.081 \text{ W/m}^2 \text{ yr}^{-1}$ (Figure 14(c)). The
779 decrease in latent heat flux indicates a reduction in the moisture carried by the air,
780 possibly as a result of decreased humidity, which further intensifies evaporation from
781 the water.

782 The sensible heat flux increases by $0.095 \text{ W/m}^2 \text{ yr}^{-1}$ (Figure 14(c)), meaning that
783 the heat exchange between the surface and the atmosphere is enhanced. This leads to
784 more evaporation, particularly during the summer when temperatures are higher.



785

786

Figure 14 Regional variations of surface net radiation and surface heat flux during 1984–2024.

787

(a) Interannual variations of mean surface net radiation; (b) multi-year mean seasonal variations of

788

surface net radiation; (c) interannual variations of mean surface heat flux; (d) multi-year mean

789

seasonal variations of surface heat flux.

790

Abbreviations: msnlwf denotes mean surface net longwave radiation; mnswwf denotes mean

791

surface net shortwave radiation; mslhf denotes mean surface latent heat flux; msshf denotes mean

792

surface sensible heat flux. The suffixes Spr, Sum, Aut, and Win represent spring, summer, autumn,

793

and winter, respectively.

794

(3) Evaporative demand and aridity conditions

795

1) Potential evapotranspiration

796

Potential evapotranspiration increases at a rate of 1.937 mm yr^{-1} (Figure 15(a)).

797

The increase in evapotranspiration directly leads to the loss of water from the lake,

798 making it an important factor contributing to the reduction in lake area. The rise in
799 potential evapotranspiration indicates that both evaporation and plant transpiration in
800 the lake area are increasing, further reducing the water volume of the lake. The increase
801 in potential evapotranspiration has a significant impact on the lake area in all time
802 periods, especially under drought and high-temperature conditions, where its effect is
803 even more pronounced.

804 2) Drought

805 The aridity index (AI) exhibits pronounced interannual variability over the study
806 period, with values generally fluctuating between approximately 0.18 and 0.40 (Figure
807 15(c)), indicating persistently dry climatic conditions in the study area. Although a
808 decreasing trend is observed (-0.0015 yr^{-1}), the trend is not statistically significant at
809 the 0.05 level ($p = 0.07$), suggesting that long-term aridity intensification is moderate
810 rather than abrupt.

811 Despite the weak linear trend, the consistently low AI values (< 0.5) confirm that
812 Bahannao Lake is located within a semi-arid to arid climatic regime, where water
813 availability is inherently limited and highly sensitive to changes in hydro-climatic
814 forcing. The wide prediction band further reflects strong year-to-year variability in
815 regional moisture conditions, likely driven by fluctuations in precipitation and
816 evaporative demand.

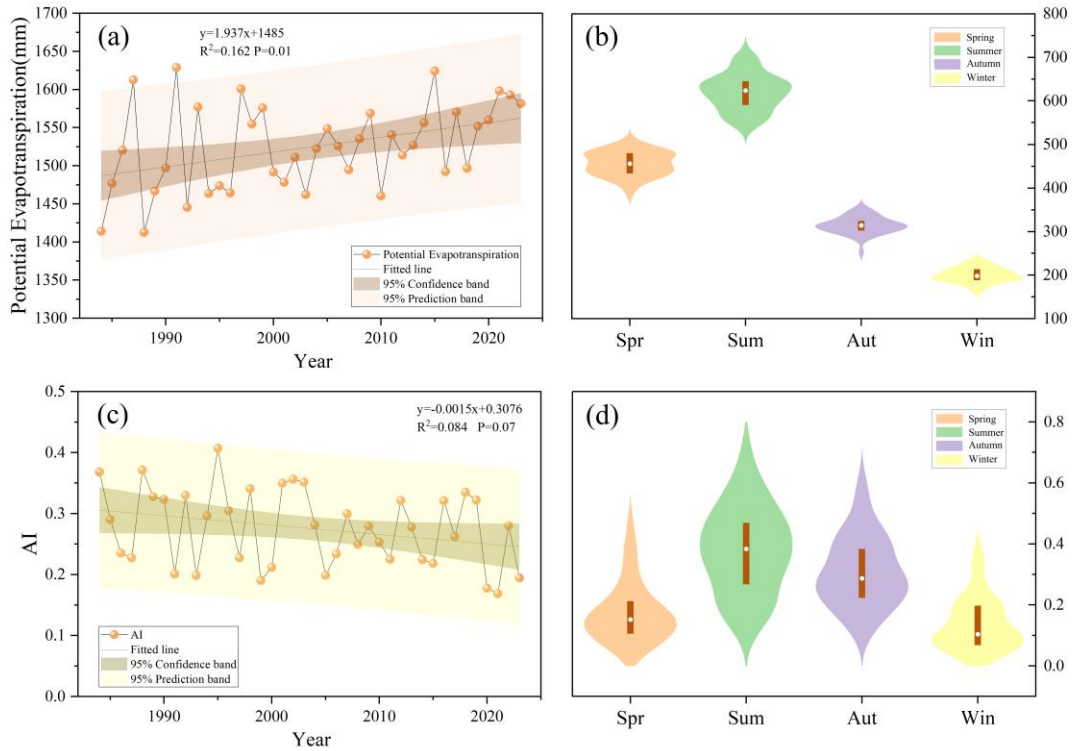
817 Importantly, the combination of a marginally decreasing AI trend and a
818 significant increase in potential evapotranspiration implies a gradual shift toward
819 enhanced atmospheric water demand, even in the absence of a statistically significant

820 drying trend in AI alone. This suggests that lake-area dynamics are more strongly
821 controlled by evaporative processes than by precipitation-driven moisture supply,
822 particularly in recent decades.

823 In addition to interannual variability, the aridity index (AI) exhibits pronounced
824 seasonal contrasts (Figure 15(d)). Summer shows the highest AI values, with a
825 relatively wide distribution and higher median, indicating comparatively wetter
826 conditions driven by concentrated precipitation during the warm season. Autumn
827 presents intermediate AI values, reflecting a transition from moisture input to increasing
828 evaporative demand.

829 In contrast, spring and winter are characterized by distinctly lower AI values.
830 Spring exhibits low median AI and limited dispersion, indicating persistent moisture
831 deficit during the lake recharge period. This seasonal dryness coincides with rising
832 temperatures and increasing evaporative demand, which constrains lake expansion
833 despite episodic precipitation events. Winter shows the lowest AI values overall,
834 reflecting extremely dry atmospheric conditions dominated by minimal precipitation
835 and suppressed moisture availability.

836 The seasonal pattern of AI highlights that Bahannao Lake is subject to strong intra-
837 annual asymmetry in hydro-climatic conditions, with relatively favorable moisture
838 supply confined to summer, while prolonged dry conditions prevail during spring and
839 winter. Such seasonal dryness amplifies the sensitivity of lake area to evaporative
840 processes.



841

842

Figure 15 Regional variations in evaporation and drought conditions during 1984–2024. (a)

843

Interannual variations of potential evapotranspiration;(b) multi-year mean seasonal variations of

844

potential evapotranspiration; (c) interannual variations of the AI; (d) multi-year mean seasonal

845

variations of the AI.

846

3.3.2 Impacts of hydro-climate elements on lake area

847

(1) Linear relationships between lake area and climatic variables

848

A sliding T-test on the lake area (Figure 16) reveals two turning points in the lake's

849

area change, specifically in 2000 and 2015. Therefore, we divide the study period into

850

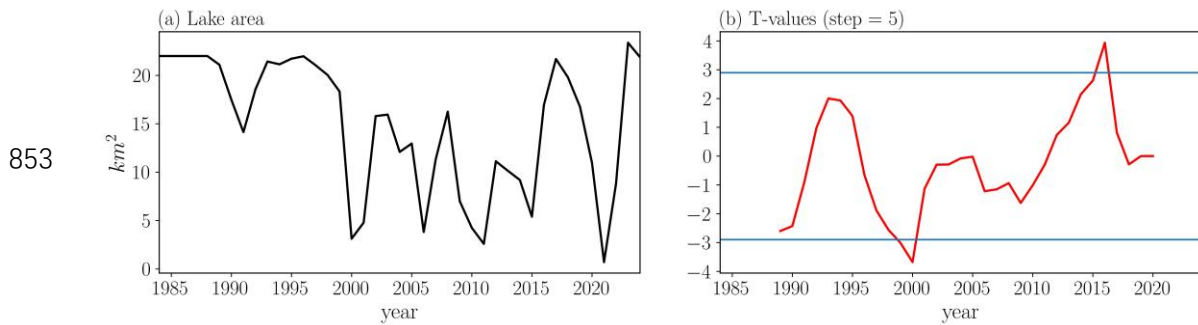
three time segments: the first period from January 1984 to December 1999, the second

851

period from January 2000 to December 2014, and the third period from January 2015

852

to July 2024, to investigate the causes of the changes in lake area.



854 Figure 16 Time series and sliding T-test of the area of the Bahannao Lake

855 The seasonal correlation analysis reveals pronounced differences in lake–climate
 856 relationships across seasons (Figure 17(a)). In spring, lake area exhibits a significant
 857 positive correlation with relative humidity (RH) ($r = 0.403$, $p < 0.01$) and a significant
 858 negative correlation with temperature (T) ($r = -0.352$, $p < 0.05$), indicating that spring
 859 lake-area variability is sensitive to atmospheric moisture conditions and warming
 860 processes. In contrast, correlations with precipitation (P) and potential
 861 evapotranspiration (PET) are weak and not statistically significant.

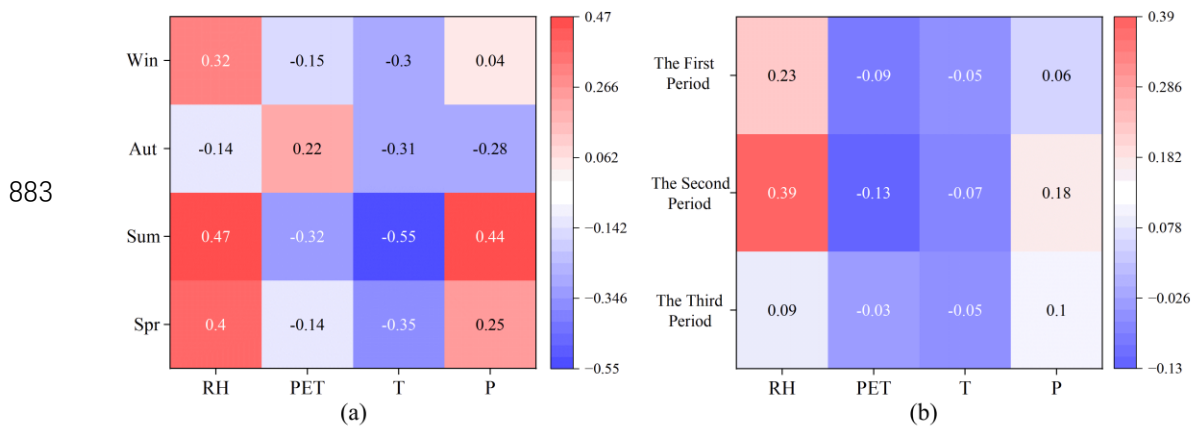
862 During summer, the lake–climate relationships are strongest. Lake area shows
 863 significant negative correlations with temperature ($r = -0.549$, $p < 0.01$) and PET ($r =$
 864 -0.315 , $p < 0.05$), and significant positive correlations with precipitation ($r = 0.437$, p
 865 < 0.01) and RH ($r = 0.468$, $p < 0.01$). These results indicate that summer lake-area
 866 variability is jointly controlled by moisture supply and enhanced evaporative demand.

867 In autumn, lake area is significantly negatively correlated only with temperature
 868 ($r = -0.315$, $p < 0.05$), whereas correlations with precipitation, RH, and PET are not
 869 significant, suggesting that autumn lake-area variations may reflect cumulative effects
 870 of antecedent hydro-climatic conditions. In winter, lake area shows a significant
 871 positive correlation with RH ($r = 0.315$, $p < 0.05$), while correlations with other climatic

872 variables remain weak, reflecting reduced hydrological activity during the cold season.

873 At the interdecadal scale, lake–climate correlations exhibit clear stage-dependent
 874 characteristics (Figure 17(b)). During the period 1984–1999, lake area shows no
 875 significant correlation with temperature, precipitation, PET, or RH, indicating a
 876 relatively weak response to individual climatic factors.

877 During 2000–2014, lake area becomes significantly positively correlated with
 878 precipitation ($p < 0.05$) and RH ($p < 0.01$), suggesting an enhanced sensitivity of lake-
 879 area variability to moisture conditions during this period. In the most recent period
 880 (2015–2024), lake area maintains a significant positive correlation only with RH ($p <$
 881 0.05), while correlations with other climatic variables weaken, implying a dominant
 882 role of atmospheric moisture conditions in regulating recent lake-area changes.



884 Figure 17 Seasonal and interdecadal differences in correlations between lake area and climatic
 885 drivers. (a) Seasonal correlations between lake area and RH, PET, T, and P. (b) Correlations between
 886 lake area and climatic variables across three sub-periods (1984–1999, 2000–2014, and 2015–2024).

887 (2) Nonlinear hydro-climatic controls revealed by XGBoost

888 To further quantify the relative importance of climatic variables and explore

889 potential nonlinear effects beyond linear correlations, an XGBoost model was applied
890 using precipitation, temperature, relative humidity, and potential evapotranspiration as
891 predictors.

892 Model evaluation indicates that training performance generally exceeds testing
893 performance, and testing R^2 values are relatively low or even negative in some cases.
894 This behavior reflects the limited sample size, strong interannual variability, and
895 inherent nonlinearity of lake-area dynamics in arid regions, rather than model
896 inadequacy. Therefore, in this study, XGBoost is primarily used as an interpretative tool
897 to assess the relative importance of climatic drivers rather than as a predictive model.

898 XGBoost-derived feature importance exhibits clear seasonal contrasts that broadly
899 agree with the correlation analysis while providing additional insights into nonlinear
900 controls (Figure 18(a)). In spring, XGBoost feature importance indicates that air
901 temperature is the most influential predictor (T, 0.31), followed by relative humidity
902 (RH, 0.28), whereas precipitation (P, 0.20) and potential evapotranspiration (PET, 0.20)
903 play secondary roles. This finding is consistent with the correlation analysis, which
904 shows a significant positive correlation between lake area and RH ($r = 0.403$, $p < 0.01$)
905 and a significant negative correlation with air temperature ($r = -0.352$, $p < 0.05$).
906 Together, these results highlight the sensitivity of springtime lake dynamics to
907 atmospheric moisture conditions and evaporative demand. Long-term trend analysis
908 further indicates a significant increase in air temperature at a rate of $0.043 \text{ }^\circ\text{C yr}^{-1}$ ($p <$
909 0.001) and a significant decline in RH (-0.099 yr^{-1} , $p = 0.009$), reinforcing the role of
910 enhanced evaporation and atmospheric drying in shaping spring lake-area changes.

911 In summer, air temperature (T, 0.35) and relative humidity (RH, 0.26) dominate
912 the feature-importance rankings, with precipitation (P, 0.18) and potential
913 evapotranspiration (PET, 0.21) also contributing substantially. This aligns well with the
914 correlation results, which indicate that summer lake area is positively correlated with
915 precipitation ($r = 0.437$, $p < 0.01$) and RH ($r = 0.468$, $p < 0.01$), and negatively
916 correlated with temperature ($r = -0.549$, $p < 0.01$) and PET ($r = -0.315$, $p < 0.05$). Trend
917 analysis shows that although precipitation exhibits a decreasing tendency (-1.736 mm
918 yr^{-1} , $p = 0.135$, not significant), PET increases significantly at a rate of 1.937 mm yr^{-1}
919 ($p = 0.01$). This suggests that summer lake-area variability is increasingly constrained
920 by enhanced evaporative demand, with the balance between water input and
921 evaporation losses playing a dominant role.

922 In autumn, linear correlations between lake area and most climatic variables are
923 weak and statistically insignificant. However, XGBoost results still indicate relatively
924 high importance for relative humidity (RH, 0.34) and potential evapotranspiration (PET,
925 0.31), suggesting that autumn lake dynamics may be governed by nonlinear processes
926 or threshold effects that are not adequately captured by linear methods alone.
927 Considering the significant upward trend in PET and the declining tendency of the
928 aridity index (AI; -0.015 yr^{-1} , $p = 0.07$), autumn lake systems appear to be transitioning
929 toward evaporation-dominated control.

930 In winter, overall feature importance values are relatively low due to reduced
931 hydrological activity, yet relative humidity (RH, 0.34) remains the most influential
932 variable in the XGBoost model. This is consistent with the correlation analysis showing

933 a significant positive relationship between winter lake area and RH ($r = 0.315$, $p < 0.05$),
934 indicating that background atmospheric moisture conditions still serve as an important
935 indicator of lake variability during the frozen period.

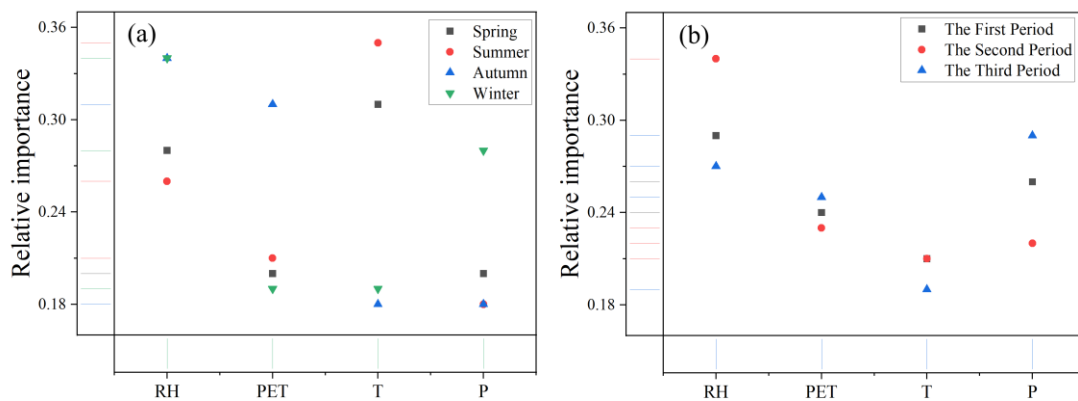
936 At the decadal scale, XGBoost results reveal a clear temporal shift in the dominant
937 climatic controls on lake-area variability, as shown in figure 18(b). During 1984–1999,
938 the importance of individual climatic variables is generally low and dispersed,
939 consistent with the weak correlations observed during this period. This suggests that
940 the lake system exhibited relatively low sensitivity to climatic fluctuations in the early
941 stage.

942 During 2000–2014, precipitation (P, 0.22), potential evapotranspiration (PET, 0.23)
943 and relative humidity (RH, 0.34) show markedly higher importance in the XGBoost
944 model, in agreement with correlation results indicating significant positive relationships
945 between lake area and precipitation ($r = 0.179$, $p < 0.05$) and RH ($r = 0.388$, $p < 0.01$).
946 This period is therefore characterized by a precipitation- and moisture-dominated
947 control regime.

948 In the most recent period (2015–2024), the importance of temperature and PET
949 increases noticeably, while the contribution of precipitation weakens. Combined with
950 the observed warming trend and enhanced evaporative demand, these results indicate a
951 transition toward an evaporation-dominated climatic control on lake-area dynamics in
952 recent years.

953 By integrating long-term trend analysis, linear correlation analysis, and XGBoost-
954 based nonlinear feature importance, this study demonstrates that lake-area variability

955 in arid regions is not governed by a single climatic factor, but rather by the interplay
 956 between water supply and evaporative demand across different seasons and time scales.
 957 Linear correlation analysis effectively captures the summer lake–climate relationship
 958 dominated by water balance, whereas the nonlinear XGBoost approach provides
 959 complementary insights into more complex control mechanisms during transitional
 960 seasons such as spring and autumn. Overall, the results indicate that with continued
 961 regional warming, increasing PET, and intensifying aridity, evaporative processes are
 962 playing an increasingly important role in controlling lake-area variability, offering
 963 important implications for understanding the response of arid-region lakes to future
 964 climate change.



966 Figure 18 Weight of influencing factors by season

967 Abbreviations: RH denotes relative humidity (%); PET denotes potential evapotranspiration (mm);
 968 T denotes air temperature (°C); P denotes precipitation (mm).

969 To further investigate the nonlinear relationships between lake area and climatic
 970 factors, partial dependence plots (PDPs) were generated for each season and period.
 971 The seasonal partial dependence plots (Fig. 19(a - p)) reveal pronounced seasonal
 972 differences and nonlinear responses of lake area to hydro-climatic variables.

973 In spring, lake area exhibits a clear threshold response to relative humidity (RH).
974 When RH remains below approximately 34 – 35%, the lake area shows only minor
975 variation. However, when RH increases to around 38 – 40%, the lake area rises rapidly,
976 indicating that enhanced atmospheric moisture conditions can significantly support lake
977 water storage. In contrast, PET shows a weak negative influence on lake area, while
978 temperature exhibits a marked decline in lake area when it approaches approximately
979 10–11 °C, suggesting that intensified evaporation may suppress lake expansion.
980 Precipitation shows only a limited influence, implying that spring lake dynamics are
981 primarily controlled by atmospheric moisture conditions and evaporative demand.

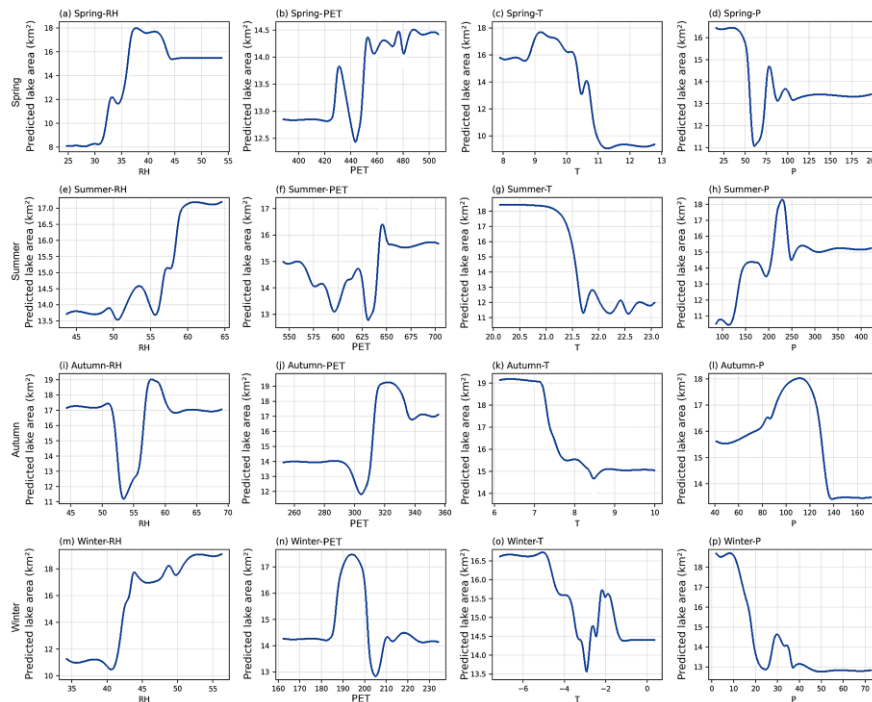
982 During summer, precipitation demonstrates a pronounced nonlinear positive effect
983 on lake area. When precipitation increases to approximately 200 mm, lake area expands
984 rapidly, indicating that rainfall represents a major water input supporting lake expansion
985 in the warm season. Relative humidity also shows a generally positive relationship with
986 lake area, whereas increasing temperature leads to a clear decline in lake area, reflecting
987 the strong evaporative effects under high-temperature conditions.

988 In autumn, lake area responds strongly to variations in PET, displaying a distinct
989 nonlinear pattern. When ET_0 approaches approximately 300 mm, lake area decreases
990 sharply, whereas at higher PET levels the lake area shows partial recovery, suggesting
991 a complex regulatory role of evaporative demand on lake water balance. Meanwhile,
992 increasing temperature generally leads to a decline in lake area, highlighting the
993 importance of evaporation processes in controlling autumn lake dynamics.

994 In winter, RH exhibits a strong positive effect on lake area. When RH increases

995 from approximately 40% to 50%, lake area increases markedly, indicating that
 996 atmospheric moisture conditions play a key role in regulating winter lake variability.
 997 Precipitation exerts a relatively weak influence, while temperature variations mainly
 998 affect lake dynamics indirectly through their influence on evaporation processes.

999 Overall, these results demonstrate that the response of lake area to hydro-climatic
 1000 variables is highly nonlinear and strongly season-dependent, with atmospheric moisture
 1001 dominating in spring and winter, precipitation controlling summer expansion, and
 1002 evaporative demand exerting a stronger influence during autumn.



1003

1004 Figure 19. Seasonal partial dependence plots (PDPs) derived from the XGBoost model.

1005 The partial dependence plots across the three periods (Figure 20(a - l)) further
 1006 reveal a clear temporal evolution in the hydro-climatic controls on lake area. During
 1007 the first period, lake area shows a strong positive response to relative humidity (RH).
 1008 When RH increases from approximately 30% to around 40%, lake area expands rapidly,

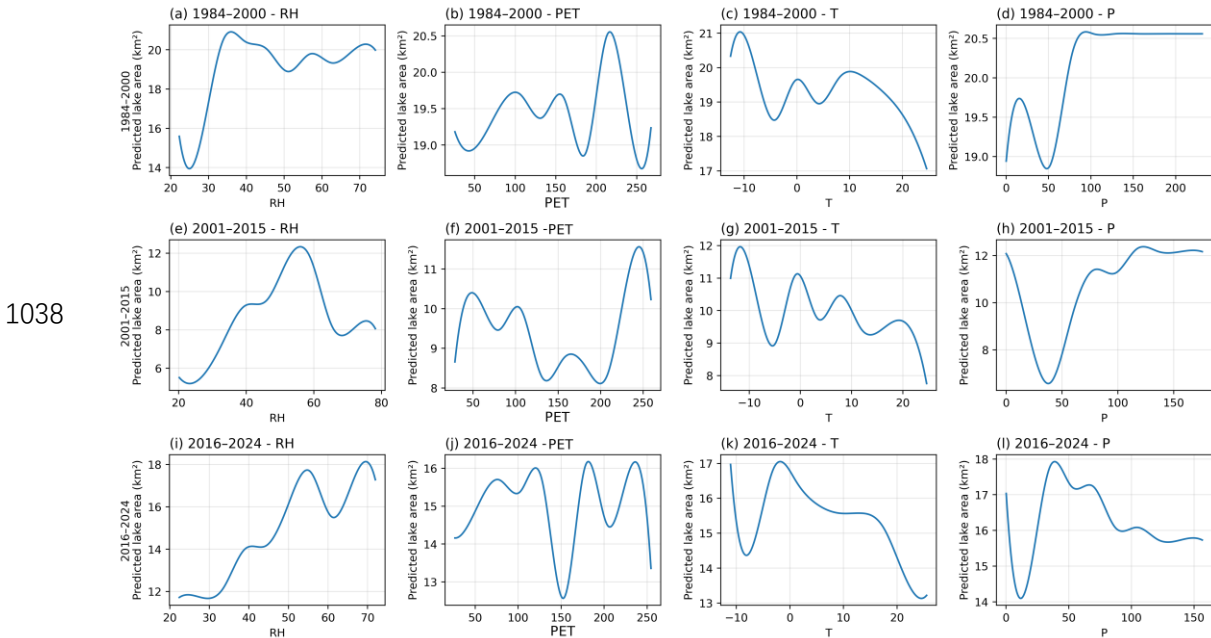
1009 indicating that atmospheric moisture conditions play a key role in sustaining lake water
1010 storage. Precipitation also exhibits a positive influence on lake area, particularly when
1011 precipitation exceeds approximately 80 - 100 mm, suggesting that water supply
1012 conditions were an important driver of lake expansion during this stage. In contrast,
1013 PET and temperature show relatively weaker influences, indicating that evaporative
1014 demand played a less dominant role during the early period.

1015 In the second period, the nonlinear responses of lake area become more complex.
1016 RH still exerts a noticeable influence on lake area, but the relationship becomes less
1017 monotonic compared with the earlier stage. Meanwhile, the influence of PET becomes
1018 more evident, suggesting that evaporative demand began to exert a stronger regulatory
1019 effect on lake dynamics. Precipitation continues to show a positive relationship with
1020 lake area, although the magnitude of the response is slightly reduced, indicating a
1021 gradual shift from water-supply dominance toward a combined influence of water
1022 supply and evaporation processes.

1023 During the most recent period, the PDPs indicate that temperature and PET exert
1024 stronger impacts on lake area variability. Increasing temperature generally leads to a
1025 decline in lake area, reflecting enhanced evaporation under warming climatic
1026 conditions. Similarly, higher PET values correspond to reduced lake area, indicating
1027 that evaporative demand has become an increasingly important control on lake
1028 dynamics. In contrast, the influence of precipitation becomes relatively weaker
1029 compared with earlier periods, suggesting that the hydrological sensitivity of the lake
1030 has gradually shifted toward stronger evaporation-driven regulation.

1031 Overall, the PDP analysis across the three periods suggests a gradual transition in
 1032 the dominant hydro-climatic controls on Bahannao Lake, shifting from moisture-
 1033 supply-dominated processes in the early period toward stronger regulation by
 1034 evaporative demand under recent warming conditions.

1035 These results highlight that lake dynamics in Bahannao Lake are governed by
 1036 complex nonlinear hydro-climatic interactions, and that the dominant climatic controls
 1037 have evolved over time.



1039 Figure 20. PDPs of hydro-climatic variables across three periods.

1040 **4. Discussion**

1041 This study constructed a continuous monthly lake-area time series for Bahannao
 1042 Lake spanning 1984–2024 using an optimized lake-area extraction framework that
 1043 integrates seasonal water-index selection, adaptive thresholding, maximum
 1044 connectivity analysis, and mutual information–based gap filling. Compared with
 1045 widely used long-term products such as the JRC Global Surface Water dataset, which

1046 are often constrained by cloud contamination, seasonal ice cover, and temporal
1047 discontinuities, the proposed framework substantially improves temporal continuity
1048 and robustness under complex environmental conditions. This improvement is
1049 particularly important for small lakes in arid and semi-arid regions, where data gaps
1050 and seasonal disturbances are pervasive in existing datasets.

1051 At the methodological level, this study introduces targeted improvements at
1052 several critical steps relative to previous approaches. First, the seasonal application of
1053 NDWI and MNDSI for non-freezing and freezing periods, respectively, enhances the
1054 stability of water-body identification under varying surface conditions, outperforming
1055 traditional single-index methods (McFeeters, 1996; Yao et al., 2015). Second, the
1056 combination of Otsu thresholding with DEM-based terrain constraints effectively
1057 reduces misclassification caused by topographic shadows and complex terrain, which
1058 is a common challenge for inland lakes in arid environments. Third, the mutual
1059 information-based image-filling strategy reconstructs cloud- and stripe-contaminated
1060 pixels by matching historically most similar cloud-free images, thereby extending the
1061 usability of long-term Landsat archives. Compared with approaches relying solely on
1062 interpolation (Zhao and Gao, 2018), this strategy substantially improves the
1063 completeness and reliability of multi-decadal lake-area records. Collectively, these
1064 methodological enhancements systematically address key challenges repeatedly
1065 identified in previous studies, including cloud contamination, seasonal variability,
1066 topographic interference, and spectral complexity of inland waters (Mouw et al., 2015;
1067 Palmer et al., 2015; Shen et al., 2017; Cao et al., 2019), and establish a transferable

1068 framework suitable for lake monitoring in arid and data-scarce regions.

1069 From a hydro-climatic perspective, the reconstructed long-term record provides
1070 important insights into the mechanisms controlling lake dynamics in arid environments.
1071 Consistent with previous studies, precipitation and evaporation emerge as the primary
1072 factors regulating lake-area variability, particularly during the warm season when both
1073 water inputs and evaporative losses are enhanced (Tao et al., 2015; Li et al., 2017). The
1074 correlation analysis indicates that lake area is significantly positively correlated with
1075 precipitation and relative humidity in summer, whereas atmospheric moisture
1076 conditions exert a more pronounced influence during spring and winter. These findings
1077 reinforce the view that lake dynamics in arid regions are governed by the seasonal
1078 balance between water supply and evaporative demand.

1079 However, compared with many existing studies that rely primarily on annual-scale
1080 analyses, the monthly lake-area time series developed here reveals pronounced seasonal
1081 heterogeneity and transitional behavior. In spring and autumn, linear correlations
1082 between lake area and individual climatic variables are generally weak, whereas
1083 XGBoost feature-importance analysis consistently identifies relative humidity and
1084 potential evapotranspiration as influential factors. This discrepancy suggests that lake
1085 responses during transitional seasons may be governed by nonlinear processes or
1086 threshold effects that cannot be fully captured by linear statistical methods alone. The
1087 combined use of correlation analysis and XGBoost therefore provides complementary
1088 perspectives on lake–climate relationships across different temporal scales.

1089 At the decadal scale, both correlation analysis and XGBoost results indicate a clear

1090 evolution in dominant climatic controls on lake-area variability. During 2000–2014,
1091 precipitation and relative humidity exhibit increased importance and significant
1092 positive associations with lake area, indicating a moisture-dominated control regime.
1093 In contrast, during 2015–2024, the importance of air temperature and potential
1094 evapotranspiration increases markedly, while the contribution of precipitation weakens.
1095 This shift reflects a transition toward evaporation-dominated control under sustained
1096 warming conditions and highlights a dynamic reorganization of hydro-climatic drivers.
1097 Such temporal evolution extends existing understanding by explicitly demonstrating
1098 how dominant controls on arid-region lakes can shift under intensified climate
1099 variability.

1100 These results have broader implications for studies of lakes in arid and semi-arid
1101 regions. The fragile water balance and limited buffering capacity of dryland lakes
1102 render them highly sensitive to even modest changes in precipitation, atmospheric
1103 moisture, and evaporative demand. The observed transition from precipitation-
1104 dominated to evaporation-dominated control suggests increasing vulnerability of arid-
1105 region lakes under ongoing climate warming. Even in the absence of a pronounced
1106 decline in precipitation, enhanced evaporation and atmospheric drying may offset or
1107 exceed water inputs, thereby accelerating lake shrinkage. This finding underscores the
1108 necessity of considering multiple hydro-climatic factors simultaneously when assessing
1109 future lake trajectories in arid environments.

1110 From a water-resources management perspective, the results indicate that lake
1111 conservation and management strategies in arid regions should not focus solely on

1112 precipitation trends but must also account for changes in evaporative demand, drought
1113 intensity, and atmospheric moisture conditions. The lake-area extraction framework and
1114 the insights into evolving climatic controls presented here provide a robust technical
1115 foundation for long-term lake monitoring, risk assessment, and adaptive water-
1116 management strategies in data-sparse dryland regions.

1117 Several limitations of this study should be acknowledged. First, while remote
1118 sensing reliably captures surface-area dynamics, subsurface processes such as
1119 groundwater inflow and outflow were not explicitly quantified and may influence lake
1120 water balance. The relatively weak correlation between lake area and precipitation
1121 observed in this study further suggests that additional hydrological processes, such as
1122 groundwater exchange or delayed runoff responses, may contribute to lake-area
1123 variability in this semi-arid environment. However, due to the lack of long-term
1124 groundwater observations in the study area, these processes could not be directly
1125 evaluated in the present study. Second, the 30 m spatial resolution of Landsat data limits
1126 detection of fine-scale shoreline changes, and future studies could benefit from
1127 integrating higher-resolution sensors such as Sentinel-2. Third, although XGBoost
1128 effectively captures nonlinear relationships, its data-driven nature limits physical
1129 interpretability relative to process-based hydrological models. Future research could
1130 integrate remote sensing, machine learning, ecohydrological modeling, and
1131 socioeconomic data to further advance understanding of lake dynamics in arid regions.

1132 **5. Conclusion**

1133 This study developed an optimized remote-sensing framework to construct a

1134 continuous monthly lake-area time series for Bahannao Lake from 1984 to 2024. By
1135 integrating seasonal water-index selection, adaptive thresholding, connectivity analysis,
1136 and mutual information-based image reconstruction, the proposed method effectively
1137 overcomes common limitations associated with cloud contamination, seasonal ice
1138 cover, and data gaps in long-term Landsat archives. Validation using Hongjiannao Lake
1139 and Wuliangshuai Lake further demonstrates the robustness and regional applicability
1140 of the framework for lake monitoring in arid and semi-arid environments.

1141 The reconstructed time series reveals pronounced interannual variability and
1142 strong seasonal contrasts in lake-area dynamics. Linear correlation analysis indicates
1143 that lake-area variations are primarily associated with precipitation and atmospheric
1144 moisture conditions during the warm season, whereas evaporative demand plays an
1145 increasingly important role during cold and transitional seasons. The combined use of
1146 correlation analysis and XGBoost modeling further reveals a clear stage-dependent
1147 evolution of climatic controls. During 1984-1999, lake dynamics were mainly
1148 associated with humidity and precipitation variability; during 2000-2014, the influence
1149 of moisture-related conditions remained important under enhanced climate variability;
1150 and during 2015-2024, rising air temperature and potential evapotranspiration emerged
1151 as dominant contributors, indicating a transition toward evaporation-dominated control
1152 under sustained warming.

1153 Overall, the results demonstrate that lake-area changes in arid regions are
1154 governed by nonlinear and evolving interactions between water supply and evaporative
1155 demand rather than by any single climatic factor. By combining high-temporal-

1156 resolution lake-area reconstruction with both linear and nonlinear analytical approaches,
1157 this study provides new insights into the mechanisms underlying arid-region lake
1158 dynamics. The proposed framework offers a valuable tool for long-term lake
1159 monitoring and contributes to improved understanding of eco-hydrological responses
1160 and water-resource vulnerability under ongoing climate change in dryland regions.

1161 **Competing interests**

1162 The authors declare that they have no conflict of interest.

1163 **Code/Data availability**

1164 The data and code that support the findings of this study are available from the
1165 corresponding author upon reasonable request.

1166 **Author contribution**

1167 R Z and X W conceived and designed the study, developed the methodology,
1168 curated the data, and performed the formal analysis. R Z was responsible for
1169 visualization. R Z and X W prepared the original draft of the manuscript, and all authors
1170 contributed to reviewing and editing the paper. X W provided overall supervision.

1171 **Acknowledgments**

1172 We are grateful to the National Key R&D Program of China (No.
1173 2023YFC3206504), National Natural Science Foundation of China (No. 52121006,
1174 41961124006), Postgraduate Thesis Fund of Nanjing Hydraulic Research
1175 Institute(Yy524010), Young Top-Notch Talent Support Program of National High-level
1176 Talents Special Support Plan, and Research Project of Ministry of Natural Resources
1177 (No. 20210103), Research Project of Inner Mongolia Academy of Science and

1178 Technology (No. 2024RCYJ05003) for providing financial support for this research..
1179 We are also thankful key authors and their agencies. We are also thankful to anonymous
1180 reviewers and editors for their helpful comments and suggestions.

1181 **References**

- 1182 Adrian, R., O' Reilly, C. M., Zagarese, H., Baines, S. B., Hessen, D. O., Keller, W., Livingstone,
1183 D. M., Sommaruga, R., Straile, D., Van Donk, E., Weyhenmeyer, G. A., and Winder, M.: Lakes
1184 as sentinels of climate change, *Limnol. Oceanogr.*, 54, 2283 – 2297,
1185 https://doi.org/10.4319/lo.2009.54.6_part_2.2283, 2009.
- 1186 Bergé-Nguyen, M. and Crétaux, J. F.: Inundations in the Inner Niger Delta: Monitoring and analysis
1187 using MODIS and global precipitation datasets, *Remote Sens.*, 7, 2127 – 2151, 2015.
- 1188 Busker, T., de Roo, A., Gelati, E., et al.: A global lake and reservoir volume analysis using a surface
1189 water dataset and satellite altimetry, *Hydrol. Earth Syst. Sci.*, 23, 669 – 690, 2019.
- 1190 Cao, Z. G., Ma, R. H., Duan, H. T., et al.: A machine learning approach to estimate chlorophyll-a
1191 from Landsat-8 measurements in inland lakes, *Remote Sens. Environ.*, 248, 111974, 2020.
- 1192 Cao, Z. G., Ma, R. H., Duan, H. T., et al.: Effects of broad bandwidth on the remote sensing of
1193 inland waters: implications for high spatial resolution satellite data applications, *ISPRS J.*
1194 *Photogramm. Remote Sens.*, 153, 110 – 122, 2019.
- 1195 Carroll, M. L., Townshend, J. R. G., DiMiceli, C. M., et al.: Shrinking lakes of the Arctic: Spatial
1196 relationships and trajectory of change, *Geophys. Res. Lett.*, 38, 2011.
- 1197 Cooley, S. W., Smith, L. C., Stepan, L., et al.: Tracking dynamic northern surface water changes
1198 with high-frequency Planet CubeSat imagery, *Remote Sens.*, 9, 1306, 2017.
- 1199 Donchyts, G., Baart, F., Winsemius, H., et al.: Earth's surface water change over the past 30 years,
1200 *Nat. Clim. Change*, 6, 810 – 813, 2016.
- 1201 Grant, L., Vanderkelen, I., Gudmundsson, L., et al.: Attribution of global lake systems change to
1202 anthropogenic forcing, *Nat. Geosci.*, 14, 849 – 854, 2021.
- 1203 Guan, L. G.: Morphological evolution and ecological function positioning of Ulansuhai Lake under
1204 the influence of human activities, *Inner Mongolia Water Resour.*, 8 – 10, 2022.
- 1205 Huang, C., Chen, Y., Zhang, S., et al.: Detecting, extracting, and monitoring surface water from

1206 space using optical sensors: A review, *Rev. Geophys.*, 56, 333 – 360, 2018.

1207 Jeppesen, E., Meerhoff, M., Davidson, T., et al.: Climate change impacts on lakes: an integrated
1208 ecological perspective based on a multi-faceted approach, with special focus on shallow lakes,
1209 *J. Limnol.*, 73, 2014.

1210 Ji, L. W., Wang, Z. W., Cui, L. L., et al.: Remote sensing monitoring of spatiotemporal dynamics of
1211 Hongjiannao Lake over the past 30 years, *Shaanxi Meteorol.*, 41 – 49, 2023.

1212 Klein, I., Gessner, U., Dietz, A. J., et al.: Global WaterPack – A 250 m resolution dataset revealing
1213 the daily dynamics of global inland water bodies, *Remote Sens. Environ.*, 198, 345 – 362, 2017.

1214 Kravitz, J., Matthews, M., Lain, L., et al.: Potential for high fidelity global mapping of common
1215 inland water quality products at high spatial and temporal resolutions based on a synthetic data
1216 and machine learning approach, *Front. Environ. Sci.*, 9, 58766, 2021.

1217 Laba, Z., Deji, Y., La, B., et al.: Remote sensing analysis on the area variations of Tangra Yutso in
1218 the Tibetan Plateau over the past 40 years, *J. Lake Sci.*, 29, 480 – 489, 2017..

1219 Li, M., Yan, D. H., Liu, S. H., et al.: Variation characteristics of water surface area and water storage
1220 capacity of Namucuo Lake in recent 40 years, *Water Resour. Power*, 35, 41 – 43, 52, 2017.

1221 Li, S., Qu, W., Zhang, T. T., et al.: Study on changes in water surface area and water volume of
1222 Ulansuhai Lake based on remote sensing imagery, *Yellow River*, 45, 22 – 23, 2023.

1223 Li, L., Long, D., Wang, Y., et al.: Global dominance of seasonality in shaping lake-surface-extent
1224 dynamics, *Nature*, 2025.

1225 Liu, Y. B., Wu, G. P., Zhao, X. S., et al.: Remote sensing for watershed hydrology: issues and
1226 challenges, *Adv. Earth Sci.*, 35, 488 – 496, 2020.

1227 Liu, Y. and Yue, H.: Analysis of Hongjiannao Lake area based on SMMI, *Sci. Technol. Eng.*, 16,
1228 122 – 127, 2016.

1229 Liu, Z. W., Su, Y. L., and Yang, L.: Limnology is a multidisciplinary and integrative science for
1230 studying inland waters: with special reference to the challenges and opportunities for the
1231 development of limnology in China, *J. Lake Sci.*, 32, 1244 – 1253, 2020.

1232 Ma, H. L., Bai, M., and Guo, Y.: Analysis on the spatiotemporal evolvement process and cause of
1233 Hongjiannao during 1957 – 2019, *Geomatics Spat. Inf. Technol.*, 43, 143 – 146, 2020.

1234 Ma, R. H., Duan, H. T., Hu, C. M., et al.: A half-century of changes in China’s lakes: global warming

1235 or human influence?, *Geophys. Res. Lett.*, 37, L24106, 2010.

1236 Ma, R. H., Yang, G. S., Duan, H. T., et al.: China' s lakes at present: number, area and spatial
1237 distribution, *Sci. China Earth Sci.*, 54, 283 – 289, 2011

1238 Ma, Y., Xu, N., Zhang, W. H., et al.: Increasing water levels of global lakes between 2003 and 2009,
1239 *IEEE Geosci. Remote Sens. Lett.*, 17, 187 – 191, 2020.

1240 McFeeters, S. K.: The use of the Normalized Difference Water Index (NDWI) in the delineation of
1241 open water features, *Int. J. Remote Sens.*, 17, 1425 – 1432, 1996.

1242 Mouw, C. B., Greb, S., Aurin, D., et al.: Aquatic color radiometry remote sensing of coastal and
1243 inland waters: challenges and recommendations for future satellite missions, *Remote Sens.*
1244 *Environ.*, 160, 15 – 30, 2015.

1245 Palmer, S. C. J., Kutser, T., and Hunter, P. D.: Remote sensing of inland waters: challenges, progress
1246 and future directions, *Remote Sens. Environ.*, 157, 1 – 8, 2015.

1247 Pekel, J. F., Cottam, A., Gorelick, N., et al.: High-resolution mapping of global surface water and
1248 its long-term changes, *Nature*, 540, 418 – 422, 2016.

1249 Pekel, J. F., Vancutsem, C., Bastin, L., et al.: A near real-time water surface detection method based
1250 on HSV transformation of MODIS multi-spectral time series data, *Remote Sens. Environ.*, 140,
1251 704 – 716, 2014.

1252 Pickens, A. H., Hansen, M. C., Hancher, M., et al.: Mapping and sampling to characterize global
1253 inland water dynamics from 1999 to 2018 with full Landsat time-series, *Remote Sens. Environ.*,
1254 243, 111792, 2020.

1255 Plug, L. J., Walls, C., and Scott, B. M.: Tundra lake changes from 1978 to 2001 on the Tuktoyaktuk
1256 Peninsula, western Canadian Arctic, *Geophys. Res. Lett.*, 35, 2008.

1257 Preston, D. L., Caine, N., McKnight, D. M., et al.: Climate regulates alpine lake ice cover phenology
1258 and aquatic ecosystem structure, *Geophys. Res. Lett.*, 43, 5353 – 5360, 2016.

1259 Råman Vinnå, L., Medhaug, I., Schmid, M., et al.: The vulnerability of lakes to climate change along
1260 an altitudinal gradient, *Commun. Earth Environ.*, 2, 35, 2021.

1261 Rossow, W. B. and Schiffer, R. A.: Advances in understanding clouds from ISCCP, *Bull. Am.*
1262 *Meteorol. Soc.*, 80, 2261 – 2288, 1999.

1263 Schmid, M., Hunziker, S., and Wüest, A.: Lake surface temperatures in a changing climate: a global

1264 sensitivity analysis, *Clim. Change*, 124, 301 – 315, 2014.

1265 Secretariat, G.: Implementation plan for the global observing system for climate in support of the
 1266 UNFCCC (2010 update), in: *Proceedings of the Conference of the Parties (COP)*, Copenhagen,
 1267 Denmark, 7 – 18, 2009.

1268 Shen, M., Duan, H. T., Cao, Z. G., et al.: Determination of the downwelling diffuse attenuation
 1269 coefficient of lake water with the Sentinel-3A OLCI, *Remote Sens.*, 9, 1246, 2017.

1270 Tan, R. J., Ma, Q., and Wang, R.: Remote sensing monitoring of long-term time-series dynamics of
 1271 water area and aquatic vegetation, Yellow River, 43, 77 – 79, 2021.

1272 Tao, S., Fang, J., Zhao, X., et al.: Rapid loss of lakes on the Mongolian Plateau, *Proc. Natl. Acad.*
 1273 *Sci. USA*, 112, 2281 – 2286, 2015.

1274 Tong, Y., Feng, L., Wang, X., et al.: Global lakes are warming slower than surface air temperature
 1275 due to accelerated evaporation, *Nat. Water*, 1, 929 – 940, 2023.

1276 Vincent, W. F.: Effects of climate change on lakes, in: *The Impact of Climate Change on European*
 1277 *Lakes*, edited by: George, D. G., Springer, Dordrecht, 55 – 60, 2009..

1278 Wang, J., Song, C., Reager, J. T., et al.: Recent global decline in endorheic basin water storages, *Nat.*
 1279 *Geosci.*, 11, 926 – 932, 2018.

1280 Wang, Y., Yan, Z. L., and Gao, F.: Monitoring spatio-temporal changes of water area in Hongjiannao
 1281 Lake from 1957 to 2015 and its driving forces analysis, *Trans. Chin. Soc. Agric. Eng.*, 34,
 1282 265 – 271, 2018..

1283 Woolway, R. I., Kraemer, B. M., Lenters, J. D., et al.: Global lake responses to climate change, *Nat.*
 1284 *Rev. Earth Environ.*, 1, 388 – 403, 2020.

1285 Xie, Z. G., Lian, Y. X., Wu, H. P., et al.: Water area change of Hongjiannao wetland from 2000 to
 1286 2018 and related policies, *Shaanxi For. Sci. Technol.*, 49, 33 – 38, 2021.

1287 Yang, G. S., Ma, R. H., Zhang, L., et al.: Lake status, major problems and protection strategy in
 1288 China, *J. Lake Sci.*, 22, 799 – 810, 2010.

1289 Yao, F., Wang, C., Dong, D., et al.: High-resolution map of urban surface water using ZY-3 multi-
 1290 spectral imagery, *Remote Sens.*, 7, 12336 – 12355, 2015.

1291 Yao, F., Wang, J., Yang, K., et al.: Lake storage variation on the endorheic Tibetan Plateau and its
 1292 attribution to climate change since the new millennium, *Environ. Res. Lett.*, 13, 064011, 2018.

- 1293 Zhang, B., Li, J. S., Shen, Q., et al.: Recent research progress on long time series and large scale
1294 optical remote sensing of inland water, *Natl. Remote Sens. Bull.*, 25, 37 – 52, 2021.
- 1295 Zhang, G. Q., Yao, T. D., Chen, W. F., et al.: Regional differences of lake evolution across China
1296 during 1960s – 2015 and its natural and anthropogenic causes, *Remote Sens. Environ.*, 221,
1297 386 – 404, 2019.
- 1298 Zhang, Y. L.: Progress and prospect in lake optics: a review, *J. Lake Sci.*, 23, 483 – 497, 2011.
- 1299 Zhao, G. and Gao, H.: Automatic correction of contaminated images for assessment of reservoir
1300 surface area dynamics, *Geophys. Res. Lett.*, 45, 6092 – 6099, 2018.
- 1301 Zhou, W., Wang, L., Li, D., et al.: Spatial pattern of lake evaporation increases under global warming
1302 linked to regional hydroclimate change, *Commun. Earth Environ.*, 2, 255, 2021.